



Available online at www.sciencedirect.com

ScienceDirect

Comput. Methods Appl. Mech. Engrg. 322 (2017) 262–295

**Computer methods
in applied
mechanics and
engineering**

www.elsevier.com/locate/cma

A finite strain integral-type anisotropic damage model for fiber-reinforced materials: Application in soft biological tissues

Farshid Fathi, Saeed Hatefi Ardakani, Peyman Fatemi Dehaghani, Soheil Mohammadi*

High Performance Computing Laboratory, School of Civil Engineering, University of Tehran, Tehran, Iran

Received 6 November 2016; received in revised form 9 April 2017; accepted 11 April 2017

Available online 8 May 2017

Highlights

- Anisotropic damage behavior of geometrically nonlinear problems is studied.
 - An integral type nonlocal damage model is utilized to circumvent the mesh dependency problem.
 - Neo-Hookean and exponential strain energy functions are exploited to capture the mechanical response of soft tissues.
 - The major role of fibers' orientation during the loading process is investigated.
-

Abstract

A large deformation finite element method is adopted to study anisotropic damage behavior of geometrically nonlinear problems with specific application in soft biological tissues. Mesh dependency, a general drawback of local damage models, is circumvented using an integral type nonlocal damage model. Three different algorithms for updating the integration search zone and the distance between the Gaussian Points are investigated to demonstrate the best solution for a large deformation based integral approach. Since there exists no record for the effect of the characteristic length of the soft biological tissues, which plays an important role in an integral type nonlocal method, this effect is also investigated. Moreover, the anisotropic highly nonlinear mechanical response of the soft fiber-reinforced tissue is captured by an exponential type strain energy function, combined with the Neo-Hookean type function, to account for distributed collagen fibers and the surrounding ground matrix. In addition, soft tissues are considered to be incompressible materials; hence, a nearly incompressible numerical model is applied to preserve the volume. Several numerical examples are presented to illustrate the accuracy and good agreement with available experimental data. The major role of fibers' orientation during the loading process is also investigated in numerical examples. It is expected to help more accurate analysis of practical cases such as aortic dissection.

© 2017 Elsevier B.V. All rights reserved.

Keywords: Integral type nonlocal damage; Anisotropic response; Hyperelastic formulation; Incompressible material; Large deformation

* Corresponding author. Fax: +98 21 6640 3808.

E-mail address: smoham@ut.ac.ir (S. Mohammadi).

1. Introduction

Accurate simulation of soft biological tissues, which involves anisotropic incompressible large deformation analysis, has been active in recent decades. From a microscopic point of view, there exists a non-uniform distribution of collagen fibers embedded in a ground of gel-like matrix with elastin fibers. Capturing the highly nonlinear mechanical response, which accounts for the fiber distribution based on the knowledge of histology, has extensively been investigated [1,2]. Due to the fact that elastin fibers are unfolded quickly after the very first steps of stretching, most of the available reports have assumed an integrated model for both the elastin fibers and the gel-like matrix [3]. Hence, a similar assumption is adopted in this study.

The isotropic gel-like ground substance, simulated based on the Neo-Hookean type hyperelastic function [4], was widely used to simulate polymeric gels and rubbers in industry [5]. This type of function was exploited in many nonlinear simulations [6] regardless of the indispensable load bearing role of collagen fibers in the secondary hardening phase of behavior of the soft tissue [7–9]. Fig. 1 schematically illustrates different phases of hardening in the mechanical response of a soft fiber-reinforced tissue.

In a pioneering work, Fung [10] proposed an exponential type function to account for the role of collagen fibers. Considering the histology of these distributed fibers and the resulting anisotropy, the shape of this exponential function was evolved in time, as reviewed by Pena [11].

Despite the fact that degradation of soft fiber-reinforced materials has an important effect in simulation of several biologically and biomechanically inspired operations, it has been addressed only by a few works so far. For instance, the role of damage and failure in studies aimed at simulation of the stent deployment procedure [12,13] or the balloon angioplasty operation [3,14] is known to be very important. Hence, a concise measure of degradation and damage distribution in the soft tissue may help a surgeon to prevent unacceptable risk of lives.

Damage mechanics accounts for the role of micro-cracks in the macroscopic response in the form of degradation of material or loss of stiffness [15]. Macroscopically, an intact material shows a regular hardening response in earlier steps of loading; however, some deviations from the normal path may later occur in the form of opening, propagation or coalescence of microstructural cracks and voids [15,16]. Mechanical properties such as inhomogeneity and anisotropy are inevitable results of the micro-mechanical geometrical alterations in cracks and voids or frictional slips [15,16]. With further propagation and coalescence of these micro-defects, discontinuous failures such as rupture and fracture may eventually occur [17].

Numerical implementation of damage phenomena and localization may suffer ill-posedness and lead to lack of objectivity. This is mainly due to occurrence of softening and degradation of material. Consequently, mesh dependency and false damage growth are possible inherent outcomes of a pure local continuum damage model. Such localizations may be influenced by the change in thermo-mechanical properties (such as microscopic defects), or by geometrical defects (such as necking or macroscopic cracking) or a combination of both.

Several remedies, such as viscose regularization methods, have been proposed to avoid such drawbacks. Nonlocal methods, introduced by Edelen and Eringen [18–21], take into consideration the strain history of the surrounding points. This idea was first proposed to address wave dispersion problem in crystalline materials [19], and then extended to elastoplastic formulation [19], smeared crack models [22,23] and softening plasticity [24]. Nonlocal continuum damage methods are categorized into two different groups: integral type formulation and gradient-enhanced models. The latter approach employs higher-order deformation gradients in constitutive formulation [25–29], and has been extended to geometrically nonlinear analysis of damage problems [17,18]. On the other hand, integral type nonlocal methods are designed in a simple way, to address the locality problem to incorporate the effects of all points within a designated radius from the reference point. Moreover, it should also be noted that one of the latest numerical approaches to avoid spurious localization is the phase-field model, which is inherently similar to the concepts of the gradient enhanced model [30,31]. Based on this approach, complex crack propagation patterns, such as branching and merging, can conveniently be resolved [30]. Dealing with soft biomechanical tissues, recently Gültekin et al. exploited the phase field model to simulate the fracture analysis of arterial walls [32].

The three dimensional finite strain work by Simo allowed for better analysis of damage concepts in soft materials [33], as followed later by Balzani et al. [34], Calvo et al. [35] and Pena [11,36]. Simo incorporated viscoelastic behavior for rubber elasticity Mooney–Rivlin type material in an isotropic damage mechanism. Afterwards, Simo and Ju presented an elastoplastic formulation based on the additive split of the stress tensor [37]. Later, a strain split damage formulation was proposed by [15], presenting a more well-posed tangent modulus than

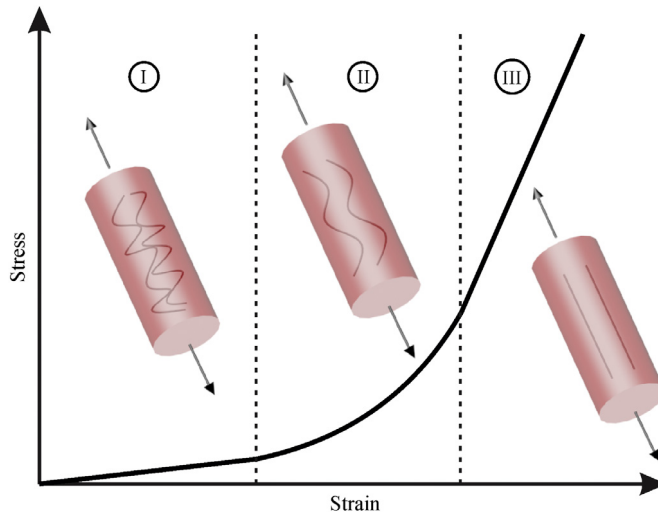


Fig. 1. Schematic representation of different hardening phases in the mechanical response of a soft fiber-reinforced tissue, stage I: folded fibers of collagen embedded in the gel-like matrix, stage II: unfolded collagen fibers, stage III: fully stretched collagen fibers.

the stress formulation. In 2006, Balzani et al. [34] exploited the discontinuous damage formulation only for fiber components. Calvo et al. [35] enhanced the general concepts of isotropic damage formalism [34] to an anisotropic discontinuous damage formulation, in which the role of both fibers and matrix was determined.

The total loss of stiffness in soft biological tissues stems from the degradation of both fiber and matrix. However, owing to the fiber's higher stiffness than the matrix, the loss of stiffness has been attributed to fiber in almost every relevant work [3,29].

Highly inspired by the work of Calvo et al. [35], Alastrué et al. [3] further investigated the anisotropic continuous damage behavior by considering an eight-chain model with crimped fiber bundles, as originally proposed by Arruda and Boyce [38]. Taking into account the rate dependency effect, Pena et al. combined the existing anisotropic damage model with viscoelasticity to capture the softening behavior in different stretch rates. They attempted to represent the role of the dominant property of rubber materials, i.e. the Mullins effect, in soft fibrous tissues with a combination of continuous and discontinuous damage formulation to achieve better convergence [39]. In 2009, Ehret and Itskov proposed a polyconvex anisotropic strain energy function to deal with softening phenomena in soft biological tissues in terms of evolution of anisotropic internal variables [40]. Later, Pena defined an internal variable for controlling the softening procedure in soft biological tissues to describe soft tissues' dominant effects such as the Mullins effect [11].

To the best knowledge of authors, none of the aforementioned works, even the recent work by Balzani et al. [41], studied the problem of mesh dependency of pure local continuum damage mechanics, which is proved to generate severe instability and loss of ellipticity [42]. Employing a relaxed incremental stress potential, however, Balzani and Ortiz [43] addressed the loss of convexity of large strain based damage formulation for fiber-reinforced materials. In a different work, a rate dependent continuum damage model was presented by Pena [36] for fibrous tissues to fully circumvent the mesh dependency by applying a viscose damage mechanism. Another attempt was presented by Waffenschmidt et al. [29] which exploited a nonlocal gradient enhanced model.

In this study, the aim is set to develop an integral type nonlocal formulation to avoid mesh dependency and to obtain higher accuracy. The effects of the non-local search zone and the *updated distance* between the point under consideration and the surrounding ones are examined. After this introduction, basics of the large deformation based kinematics of soft biological tissues are presented in Section 2. Section 3 presents the anisotropic damage model and its related formulation. Furthermore, an efficient damage function is introduced to be fitted easily to various sets of data. In addition, three different algorithms are incorporated to define the nonlocal integral type formulation. Section 4 is devoted to numerical examples, followed by the concluding remarks.

2. Continuum framework

Soft biological tissues undergo large deformations, and ligaments, arteries, skin and many other soft tissues may well be considered as *hyperelastic* materials. Hyperelasticity describes the behavior of a material in a point as a pure function of the deformation of that point [44,45].

A body in the initial configuration Ω_0 at time $t = 0$ is mapped through an arbitrary motion φ to the current configuration Ω at time t . Assuming a point on the initial configuration ($\mathbf{X} \in \Omega_0$) and the corresponding one on the current configuration ($\mathbf{x} \in \Omega$), the deformation gradient \mathbf{F} is defined as [45]

$$d\mathbf{x} = \mathbf{F}d\mathbf{X}, \quad \mathbf{F}(\mathbf{X}) = \nabla\varphi_t(\mathbf{X}). \quad (1)$$

The corresponding right Cauchy tensor \mathbf{C} is defined as [45]

$$\mathbf{C} = \mathbf{F}^T \mathbf{F}. \quad (2)$$

The *Jacobian*, which is a measure of the volume change, $J = \frac{dv}{dV} = \det(\mathbf{F}) > 0$ [45], is an important parameter in describing the behavior of soft biological tissues. For hyperelastic models which undergo large deformations, the volume changes drastically in a general compressible formulation. However, for simulation of nearly incompressible soft tissues, the incompressibility condition is imposed via an external pressure to preserve the volume ($J \approx 1$). This external pressure is numerically implemented by a penalty method [3,7,35]. Following the general formalism of multiplicative decomposition for incompressible materials, the deformation gradient and, consequently, the strain energy function (SEF) are decomposed into dilational (volumetric) and deviatoric parts [45]. The deviatoric part has no effect on the volume preservation, and only the pressure confines the volumetric part. The deviatoric parts of the deformation gradient and the corresponding right Cauchy tensor are defined as [45]

$$\tilde{\mathbf{F}} = J^{-1/3} \mathbf{F}, \quad \tilde{\mathbf{C}} = J^{-2/3} \mathbf{C}. \quad (3)$$

Previously mentioned, soft biological tissues are considered as anisotropic fiber reinforced composites in which the surrounding matrix constitutes the isotropic part and the anisotropy stems from the dispersed fibers. Most of the works in literature assumed sets of transversely isotropic distribution [46] for these fibers, known as *fiber families* [7]. As a widespread assumption, muscular type tissues are typically composed of only one family, whereas there are two or three families for tissues with randomly distributed fibers (such as skin) based on the texture of the tissue. For the isotropic part of formulation, three frequently used standard invariants, [7,9,45] are adopted

$$I_1 = \text{tr}(\mathbf{C}), \quad (4a)$$

$$I_2 = \text{tr}(\text{cof}(\mathbf{C})) \quad (4b)$$

$$I_3 = \det(\mathbf{C}). \quad (4c)$$

Adopting vectors \mathbf{a}_0 and \mathbf{b}_0 to define directions of the anisotropic two-family type formulation, invariants I_4 and I_6 are introduced to consider the role of fibers in SEFs [9,11],

$$I_4 = \text{tr}(\mathbf{C} \cdot \mathbf{M}) \quad (4d)$$

$$I_6 = \text{tr}(\mathbf{C} \cdot \mathbf{N}) \quad (4e)$$

where $\mathbf{M} = \mathbf{a}_0 \otimes \mathbf{a}_0$ and $\mathbf{N} = \mathbf{b}_0 \otimes \mathbf{b}_0$ are the structural tensors corresponding to the direction of each fiber family. Finally, a two family type SEF for fiber reinforced tissues can be rewritten as [35]

$$\Psi(\mathbf{C}, \mathbf{M}, \mathbf{N}) = \Psi^{\text{vol}}(J) + \tilde{\Psi}^{\text{iso}}(\tilde{\mathbf{C}}) + \tilde{\Psi}^{\text{anis}}(\tilde{\mathbf{C}}, \mathbf{M}, \mathbf{N}). \quad (5)$$

The second Piola–Kirchhoff and the corresponding elasticity tensor are obtained from the decomposed SEF [35],

$$\mathbf{S} = \frac{\partial \Psi}{\partial \mathbf{E}} = 2 \frac{\partial \Psi}{\partial \mathbf{C}} = \mathbf{S}^{\text{vol}} + \tilde{\mathbf{S}}^{\text{iso}} + \tilde{\mathbf{S}}^{\text{anis}} \quad (6)$$

$$\mathcal{C} = \frac{\partial^2 \Psi}{\partial \mathbf{E} \partial \mathbf{E}} = 4 \frac{\partial^2 \Psi}{\partial \mathbf{C} \partial \mathbf{C}} = \mathcal{C}^{\text{vol}} + \tilde{\mathcal{C}}^{\text{iso}} + \tilde{\mathcal{C}}^{\text{anis}} \quad (7)$$

where \mathbf{E} is the Green–Lagrange strain tensor, $\mathbf{E} = (\mathbf{C} - \mathbf{I})/2$.

The spatial description of Eqs. (6) and (7) is also required for the updated lagrangian formulation (see Appendix A) [44]. Hence, the Cauchy stress and the spatial elasticity tensor can be derived by the push forward operation as [45]

$$\sigma = J^{-1} \chi_*(\mathbf{S}), \quad \sigma_{ij} = J^{-1} \mathbf{F}_{ik} \mathbf{F}_{jl} \mathbf{S}_{kl} \quad (8)$$

$$\epsilon = J^{-1} \chi_*(\mathcal{C}), \quad \epsilon_{ijkl} = J^{-1} \mathbf{F}_{iI} \mathbf{F}_{jJ} \mathbf{F}_{kK} \mathbf{F}_{lL} \mathcal{C}_{IJKL}. \quad (9)$$

Further details regarding the explicit derivation scheme and spatial formulations can be found in [45,47].

3. Anisotropic damage model

3.1. Finite strain based hyperelastic damage model

An uncoupled formulation explaining the degradation criterion of soft tissues is presented in this section. A scalar damage model is adopted for each component of biological tissues in a way that only affects the deviatoric part of the energy density. Applying the damage parameter into SEF of Eq. (5) leads to

$$\Psi(\mathbf{C}, \mathbf{M}, \mathbf{N}, D_k) = \Psi^{\text{vol}}(J) + (1 - D_k) \tilde{\Psi}_0^k(\tilde{\mathbf{C}}, \mathbf{M}, \mathbf{N}); \quad k = m, f_1, f_2 \quad (10)$$

where m stands for the surrounding matrix as the isotropic part, f_1 and f_2 are families of fibers, representing the anisotropic role in the soft tissue and the subscript zero in $\tilde{\Psi}_0^k$ denotes the intact material. In the realm of macroscopic continuum, the second law of thermodynamics requires the internal dissipation to be nonnegative. In an isothermal process, the Clausius–Duhem inequality reflects this requirement as

$$\mathbf{S} : \dot{\mathbf{E}} - \dot{\Psi} \geq 0 \quad (11)$$

where

$$\dot{\Psi} = \frac{d\Psi^{\text{vol}}(J)}{dJ} j - \tilde{\Psi}_0^k \dot{D}_k + (1 - D_k) \frac{\partial \tilde{\Psi}_0^k}{\partial \tilde{\mathbf{C}}} : \dot{\tilde{\mathbf{C}}}; \quad \dot{\mathbf{C}} = 2\dot{\mathbf{E}} \quad (12)$$

putting Eq. (12) into the inequality (11) with some manipulations yields

$$\left\{ \mathbf{S} - J \frac{d\Psi^{\text{vol}}(J)}{dJ} \mathbf{C}^{-1} - J^{-2/3} P : (1 - D_k) 2 \frac{\partial \tilde{\Psi}_0^k}{\partial \tilde{\mathbf{C}}} \right\} : \frac{\dot{\tilde{\mathbf{C}}}}{2} + \tilde{\Psi}_0^k \dot{D}_k \geq 0 \quad (13)$$

where the fourth order tensor P is

$$\mathbf{P} = \tilde{\mathbf{I}} - \frac{1}{3} \tilde{\mathbf{C}}^{-1} \otimes \tilde{\mathbf{C}}; \quad \tilde{\mathbf{I}}_{ijkl} = \frac{1}{2} (\delta_{ik} \delta_{jl} + \delta_{il} \delta_{jk}). \quad (14)$$

Material's incompressibility ($J \approx 1$) requires the following expression throughout the deformation

$$j = \frac{1}{2} J \mathbf{C}^{-1} : \dot{\mathbf{C}} = 0. \quad (15)$$

Satisfying both the constraint equation (15) and the first term of the inequality (13), the damage induced second Piola–Kirchhoff stress can be presented as,

$$\mathbf{S} = \mathbf{S}^{\text{vol}} + (1 - D_k) \tilde{\mathbf{S}}_0^k; \quad k = m, f_1, f_2. \quad (16)$$

The other equation which stems from the second term of the dissipation inequality (13) yields to the thermodynamic driving force, which is work conjugate to the internal variable D_k ,

$$f_k \dot{D}_k \geq 0; \quad f_k = \tilde{\Psi}_0^k(\tilde{\mathbf{C}}) = - \frac{\partial \Psi}{\partial D_k} \quad (17)$$

where f_k governs the damage evolution.

3.2. Damage evolution function

Several works have utilized an exponential type damage function for the evolution law, which governs the material regardless of its ductility and texture [11,17,33,35]. In this paper, a similar exponential type function is exploited which properly imposes monotonicity, well-posedness and numerical stability with the minimum number of parameters [48]. In his pioneering works, Simo invoked a typical terminology based on the yielding surface of plasticity to formulate a viscoelastic damage formulation in the strain space. Here, the Simo's model, which is applicable to both inviscid and viscose models, is described. The evolution (or equivalent strain) parameter at time $s \in \mathbb{R}^+$, which rules the damage criterion is presented as [33]

$$\bar{E}_s^k = \sqrt{2\tilde{\Psi}_0^k(\tilde{\mathbf{C}}(s))}; \quad k = m, f_1, f_2. \quad (18)$$

The maximum experienced value of the evolution parameter is of paramount importance since it determines the damage condition. The maximum value of the evolution parameter up to the current time t is formulated as [33]

$$\bar{E}_t^k = \max_{s \in (-\infty, t]} \sqrt{2\tilde{\Psi}_0^k(\tilde{\mathbf{C}}(s))}; \quad k = m, f_1, f_2. \quad (19)$$

Finally, the loading or unloading condition is governed by the damage criterion

$$\Phi_k(\mathbf{C}(t), \bar{E}_t^k) = \sqrt{2\tilde{\Psi}_0^k(\tilde{\mathbf{C}}(t))} - \bar{E}_t^k \leq 0. \quad (20)$$

A damage surface is defined based on the zero damage criterion in the strain space

$$\left\{ \begin{array}{ll} \Phi_k < 0 & \text{elastic} \\ \Phi_k = 0 \rightarrow \begin{cases} \mathbf{N}_k : \frac{\dot{\mathbf{C}}}{2} < \mathbf{0} & \text{elastic unloading} \\ \mathbf{N}_k : \frac{\dot{\mathbf{C}}}{2} = \mathbf{0} & \text{neutral loading} \\ \mathbf{N}_k : \frac{\dot{\mathbf{C}}}{2} > \mathbf{0} & \text{damage loading} \end{cases} & k = m, f_1, f_2 \end{array} \right. \quad (21)$$

where \mathbf{N}_k is the normal to the damage surface ($\mathbf{N}_k = \partial \Phi^k / \partial \mathbf{E} = (1/\bar{E}_s^k) \partial \tilde{\Psi}_0^k / \partial \mathbf{E}$) [33]. Evolution of the damage variable D_k is characterized by an evolution function $\tilde{H}^k(\bar{E}^k, D_k)$, which results in an irreversible rate equation presented by [33],

$$\frac{dD_k}{dt} = \begin{cases} \tilde{H}^k(\bar{E}^k, D_k) \dot{\bar{E}}^k & \text{if } \Phi_k = 0 \text{ and } \mathbf{N}_k : \frac{\dot{\mathbf{C}}}{2} > \mathbf{0} \\ 0 & \text{otherwise.} \end{cases} \quad (22)$$

Assuming the arbitrary value of \tilde{H}^k to be independent of the damage variable D_k leads to a numerically more convenient and straightforward damage function, $\tilde{G}(\bar{E}^k)$,

$$\tilde{H}^k(\bar{E}^k) = -d\tilde{G}^k(\bar{E}^k)/d\bar{E}^k. \quad (23)$$

The corresponding second Piola–Kirchhoff (16) can now be rewritten as

$$\begin{aligned} \mathbf{S} &= \mathbf{S}^{\text{vol}} + \tilde{G}^k(\bar{E}_t^k) \tilde{\mathbf{S}}_0^k; \\ \tilde{\mathbf{S}}_0^k &= \frac{\partial \tilde{\Psi}_0^k}{\partial \mathbf{E}} = 2 \frac{\partial \tilde{\Psi}_0^k}{\partial \mathbf{C}}; \quad \bar{E}_t^k = \max_{s \in (-\infty, t]} \sqrt{2\tilde{\Psi}_0^k(\tilde{\mathbf{C}}(s))}; \quad k = m, f_1, f_2. \end{aligned} \quad (24)$$

The evolution function is adopted in a way to uncouple \tilde{H}^k from D_k [11,29,33,35,36]. Exponential or hyperbolic functions have been utilized in the literature, i.e. in the form of $\tilde{G}(\bar{E}^k) = 1 - D_k = \exp[\alpha(\bar{E}_0^k - \bar{E}^k)]$. For a brief and good summary of these functions refer to [29,48].

3.3. Damage induced elasticity tensor

Applying the chain rule to Eq. (24), the deviatoric part of the second Piola–Kirchhoff tensor can be written as [33]

$$\dot{\tilde{\mathbf{S}}}^k = \tilde{\mathbf{C}}^k : \dot{\mathbf{E}} = \begin{cases} \left[\tilde{G}^k \tilde{\mathbf{C}}_0^k + \tilde{G}'^k \tilde{\mathbf{S}}_0^k \otimes \tilde{\mathbf{S}}_0^k \right] : \dot{\mathbf{E}} & \text{if } \Phi_k = 0 \text{ and } \mathbf{N}_k : \frac{\dot{\mathbf{C}}}{2} > \mathbf{0} \\ \tilde{G}^k \tilde{\mathbf{C}}_0^k : \dot{\mathbf{E}} & \text{otherwise} \end{cases} \quad (25)$$

where $\tilde{G}'^k = d\tilde{G}^k/d\bar{\underline{E}}^k = -\bar{H}^k$. The volumetric part of the elasticity tensor is similar to Eq. (7). The damage induced deviatoric part is then formulated based on Eq. (25) as

$$\tilde{\mathbf{C}}^k = \begin{cases} \tilde{G}^k \tilde{\mathbf{C}}_0^k + \tilde{G}'^k \tilde{\mathbf{S}}_0^k \otimes \tilde{\mathbf{S}}_0^k & \text{if } \Phi_k = 0 \text{ and } \mathbf{N}_k : \frac{\dot{\mathbf{C}}}{2} > \mathbf{0} \\ \tilde{G}^k \tilde{\mathbf{C}}_0^k & \text{otherwise.} \end{cases} \quad (26)$$

3.4. Integral-type nonlocal damage continuum

As mentioned earlier, there exist a few works in available biological contributions which attempted to circumvent mesh dependency by exploiting the viscoelastic [36], the relaxed incremental variational formulation [43], and the nonlocal gradient formulation [29]. Here, however, a nonlocal integral type formulation is employed to address the problem of mesh dependency. The present integral type nonlocal damage method incorporates neighboring points to evaluate an equivalent strain, avoiding local measures from governing the global failure [49].

In this study, since evolution parameter and consequently the damage criterion are independent of the damage parameter, implementing a coupled solution is not required. On the other hand, in a gradient enhanced scheme, a second independent weak formulation has to be solved, which results in a coupled solution with increased degrees of freedom and larger system of equations. Furthermore, a fully coupled or staggered solution has to be taken into account in order to solve the proposed coupled equations which may result in the oscillation of convergence.

Based on the work by Jirásek [50], the nonlocal evolution parameter is presented as an average value to circumvent localization,

$$\bar{\underline{E}}_{\text{non}}^k(\xi) = \int_v a(\xi, \xi) \bar{\underline{E}}_s^k(\xi) d\xi \quad (27)$$

where $\bar{\underline{E}}_{\text{non}}^k$ and $\bar{\underline{E}}_s^k$ are the average equivalent nonlocal parameter and the corresponding local parameter, respectively. ξ and ξ are the locations of the so called “target” point and the “source” points, respectively, and $r = \|\xi - \xi\|$ defines the distance between these two points. Furthermore, $a(\xi, \xi)$ is the nonlocal weight function defined as [50].

$$a(\xi, \xi) = \frac{a_0(\|\xi - \xi\|)}{\int_v a_0(\|\xi - \vartheta\|) d\vartheta} \quad (28)$$

a_0 denotes a polynomial function [50]

$$a_0(r) = \left(1 - \frac{r^2}{R^2} \right)^2 \quad (29)$$

where $\langle \bullet \rangle$ denotes the nonnegative Macaulay bracket defined as $\langle \bullet \rangle = [| \bullet | + \bullet] / 2$. Finally, R is a scalar related to the intrinsic length scale, and is defined as the largest possible distance of point ξ from the reference point ξ . Parameter ϑ represents the integration variable. A schematic illustration of the nonlocal integration process is presented in Fig. 2.

Fig. 2 shows that a smooth response can be obtained by the method proposed by Bazant and Jirásek [51] as an average solution of the oscillatory response. $\bar{\underline{E}}(\xi)$ can be interpreted as the micro-fluctuation of the evolution parameter in the microstructural anisotropic response. It is smoothed in the form of averaged (integrated) $\bar{\underline{E}}_{\text{non}}$ of the macro-structural response. This nature of smoothness in integral-type methods helps creating a more straightforward solution compared with the gradient-type methods; hence, a nonlocal integral-type solution is adopted here. It should

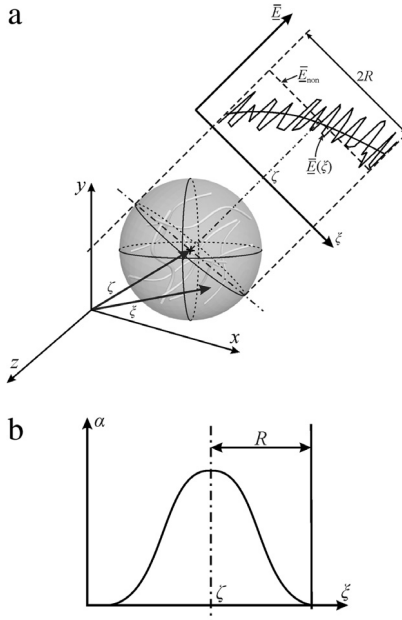


Fig. 2. (a) Integration procedure to consider the effects of gauss points within the interaction radius, (b) quartic weight function with the interaction radius of R .

Source: Adopted from the original idea by Bazant and Jirásek (2002) [51].

be noted that exploiting the gradient enhanced methods allows for successful capture of severe oscillatory and highly localized response by solving another weak form apart from the equilibrium equation [29,52]. A fully coupled or a staggered method has to be taken into account, which increases the computational cost. Furthermore, the gradient enhanced methods have reportedly led to sensitive results in damage and plasticity problems [53,54].

Table 1 presents the adopted algorithm for implementation of the nonlocal anisotropic damage model.

The fourth step of **Table 1**, which is the numerical implementation of Eqs. (27)–(29) and the update procedure, is presented in **Table 2**. The first algorithm is the classical nonlocal method for small strain formulation, in which the search zone and the weight factors based on relative distances are predetermined. In other words, the candidate Gaussian Points in the search zone and their relative distances are determined in the initial configuration and before the first step of analysis. These data remain unchanged during the solution process within a total lagrangian formulation in the reference configuration. It is postulated by Jirásek [50] that, in a small strain based finite element analysis, Eqs. (27) and (28) remain constant during the analysis. Hence, there is no need to calculate these parameters in every iteration of every step. However, for simulations that undergo large deformations, considerable changes in relative distances between Gaussian points are probable, and may substantially change the weight functions in Eq. (27).

Updating the locations of Gaussian points, and the influence of corresponding weight factors on the integration process are investigated in the second algorithm based on the updated lagrangian method. In the third algorithm, the search zone is also updated in each step of deformation in order to determine possible deviations in number of integration points under consideration in each step. The procedure of selection of integration points stems from the inherently chosen radius of the sphere centered at the specific point of consideration. The importance of the third algorithm will be revealed when the domain undergoes drastically large relative deformations or out of plane flexural deformations.

4. Numerical simulations

Wide spectrum of numerical examples is investigated in this study. The first two examples are devoted to the uniaxial test to examine the fitting capability of the proposed damage function to capture various experimental data.

Table 1

Algorithm for anisotropic damage model.

(1)	Given parameters at each Gaussian point: deformation gradient \mathbf{F}_{n+1} , local evolution parameter $\bar{\mathbf{E}}_{t_n}^k$ and damage parameter D_{k_n}
(2)	Compute the contribution of strain energy function $\Psi_{0_{n+1}}$, $\mathbf{S}_{0_{n+1}}$ and $\mathcal{C}_{0_{n+1}}$ for the intact material
(3)	Compute the current local evolution parameter $\bar{\mathbf{E}}_{s_{n+1}}^k$ based on (18) $\bar{\mathbf{E}}_{s_{n+1}}^k = \sqrt{2\tilde{\Psi}_{0_{n+1}}^k(\tilde{\mathbf{C}}(s))}$
(4)	Compute the nonlocal measures of evolution parameters based on Table 2
(5)	Check the damage criterion based on (20), (21) IF $\Phi_{k_{n+1}} = \bar{\mathbf{E}}_{\text{non}_{n+1}}^k - \bar{\mathbf{E}}_{t_{n+1}}^k < 0$ $D_{k_{n+1}} = D_{k_n}$ ELSE Update the damage parameter based on (Eq. (31)) $D_{k_{n+1}} = 1 - \begin{cases} 1 & \text{if } \bar{\mathbf{E}}_{t_{n+1}}^k < \bar{\mathbf{E}}_{\min}^k \\ \frac{\bar{\mathbf{E}}_{\max}^k - \bar{\mathbf{E}}_{t_{n+1}}^k}{\bar{\mathbf{E}}_{\max}^k - \bar{\mathbf{E}}_{\min}^k} \exp[(\beta_k \frac{\bar{\mathbf{E}}_{t_{n+1}}^k - \bar{\mathbf{E}}_{\min}^k}{\bar{\mathbf{E}}_{\min}^k - \bar{\mathbf{E}}_{\max}^k})] & \text{if } \bar{\mathbf{E}}_{\min}^k \leq \bar{\mathbf{E}}_{t_{n+1}}^k \leq \bar{\mathbf{E}}_{\max}^k \\ 0 & \text{if } \bar{\mathbf{E}}_{t_{n+1}}^k > \bar{\mathbf{E}}_{\max}^k \end{cases}$ ENDIF
(6)	Compute the stress tensor IF solver = “no update” $\mathbf{S}_{n+1} = \mathbf{S}_{n+1}^{\text{vol}} + (1 - D_{k_{n+1}})\tilde{\mathbf{S}}_{0_{n+1}}^k; k = m, f_1, f_2$ ELSEIF solver = “updated distance” or “updated distance and search” (see Eq. (8)) $\sigma_{n+1} = \sigma_{n+1}^{\text{vol}} + (1 - D_{k_{n+1}})\tilde{\sigma}_{0_{n+1}}^k; k = m, f_1, f_2$ ENDIF
(7)	Compute the elastic modulus IF solver = “no update” $\mathcal{C}_{n+1}^k = \mathcal{C}_{\text{vol}_{n+1}}^k + (1 - D_{k_{n+1}})\tilde{\mathcal{C}}_{0_{n+1}}^k - \tilde{H}_{n+1}^k \tilde{\mathbf{S}}_{0_{n+1}}^k \otimes \tilde{\mathbf{S}}_{0_{n+1}}^k; k = m, f_1, f_2$ ELSEIF solver = “updated distance” or “updated distance and search” (see Eq. (9)) $\epsilon_{n+1}^k = \epsilon_{\text{vol}_{n+1}}^k + (1 - D_{k_{n+1}})\tilde{\epsilon}_{0_{n+1}}^k - \tilde{H}_{n+1}^k \tilde{\mathbf{S}}_{0_{n+1}}^k \otimes \tilde{\mathbf{S}}_{0_{n+1}}^k; k = m, f_1, f_2$ where $\tilde{\mathbf{S}}$ is the push forward measure of $\tilde{\mathbf{S}}$ based on Eq. (9) ENDIF
(8)	Compute displacements from the finite element solution IF solver = “no update” Solve the total lagrangian equilibrium equation based on Eqs. (A.5)–(A.8): $(\mathbf{K}_L + \mathbf{K}_{NL})\mathbf{u} = \mathbf{R} - \mathbf{R}_i$ ELSEIF solver = “updated distance” or “updated distance and search” Solve the updated lagrangian equilibrium equation based on Eqs. (A.10)–(A.13): $(\mathbf{K}_L + \mathbf{K}_{NL})\mathbf{u} = \mathbf{R} - \mathbf{R}_i$ ENDIF

The next two examples are designed to demonstrate the efficiency of the adopted nonlocal type damage model to avoid mesh dependency. Finally, application of this damage model in a practical problem is comprehensively investigated. Targeting these goals, the most general form of SEF based on Eq. (10) is adopted [35],

$$\begin{aligned} \Psi = K \ln J^2 + (1 - D_m) \left\{ c_1 (\tilde{I}_1 - 3) + c_2 (\tilde{I}_2 - 3) \right\} \\ + (1 - D_{f_i}) \frac{c_3}{2c_4} \left\{ \exp \left[c_4 \left(\kappa_i \tilde{I}_1 + [1 - 3\kappa_i] \tilde{I}_{f_i} - I_{0_i} \right)^2 \right] - 1 \right\} \quad i = 1, 2 \end{aligned} \quad (30)$$

where K, c_1, c_2, c_3 and c_4 are material parameters, and $\tilde{I}_{f_1} = \tilde{I}_4$ and $\tilde{I}_{f_2} = \tilde{I}_6$ are deviatoric invariants. The dispersion factor κ is defined according to a π -periodic von Mises distribution [1] in the range of $0 \leq \kappa \leq 1/3$. This parameter

Table 2

Algorithm for numerical implementation of nonlocal averaging formulation based on three different updating schemes.

(1)	Compute local evolution parameter values, \bar{E}_s^k , at each gauss point
(2)	<p>IF solver = “no update”</p> <ul style="list-style-type: none"> • Set the initial global locations of gauss points (based on Eq. (A.1) in the total lagrangian formulation): $\mathbf{X}_{\text{initial}} = \sum_{a=1}^{N_{\text{node}}} \mathbf{N}_a(\xi_1^{GP}, \xi_2^{GP}, \xi_3^{GP}) \mathbf{X}_{a\text{initial}}$ where $\mathbf{X}_{a\text{initial}}$ are the initial nodal coordinates, and ξ_1^{GP}, ξ_2^{GP} and ξ_3^{GP} are the locations of gauss points in the natural coordinates. • Set the initial search for candidate gauss points within the characteristic length in the initial configuration. • Set the Jacobian based on the initial configuration: $J = J_{\text{initial}} = \frac{\partial \mathbf{X}_{\text{initial}}}{\partial \xi}; \frac{\partial \mathbf{N}}{\partial \mathbf{X}_{\text{initial}}} = J_{\text{initial}}^{-1} \frac{\partial \mathbf{N}}{\partial \xi}$
(3)	<p>ELSEIF solver = “updated distance”</p> <ul style="list-style-type: none"> • Compute the global locations of gauss points (based on Eq. (A.1) in the updated lagrangian formulation): $\mathbf{X}_{\text{current}} = \sum_{a=1}^{N_{\text{node}}} \mathbf{N}_a(\xi_1^{GP}, \xi_2^{GP}, \xi_3^{GP}) \mathbf{X}_{a\text{current}}$ where $\mathbf{X}_{a\text{current}}$ are the updated nodal coordinates, and ξ_1^{GP}, ξ_2^{GP} and ξ_3^{GP} are the locations of gauss points in the natural coordinates. • Set the initial search for candidate gauss points within the characteristic length in the current configuration. • Compute the Jacobian based on the current configuration: $J = J_{\text{current}} = \frac{\partial \mathbf{X}_{\text{current}}}{\partial \xi}; \frac{\partial \mathbf{N}}{\partial \mathbf{X}_{\text{current}}} = J_{\text{current}}^{-1} \frac{\partial \mathbf{N}}{\partial \xi}$
(4)	<p>ELSEIF solver = “updated distance and search”</p> <ul style="list-style-type: none"> • Compute the global locations of gauss points (based on Eq. (A.1) in the updated lagrangian formulation): $\mathbf{X}_{\text{current}} = \sum_{a=1}^{N_{\text{node}}} \mathbf{N}_a(\xi_1^{GP}, \xi_2^{GP}, \xi_3^{GP}) \mathbf{X}_{a\text{current}}$ where $\mathbf{X}_{a\text{current}}$ are the updated nodal coordinates, and ξ_1^{GP}, ξ_2^{GP} and ξ_3^{GP} are the locations of gauss points in the natural coordinates. • Employ a new search for candidate gauss points within the characteristic length in the current configuration. • Compute the Jacobian and based on the current configuration: $J = J_{\text{current}} = \frac{\partial \mathbf{X}_{\text{current}}}{\partial \xi}; \frac{\partial \mathbf{N}}{\partial \mathbf{X}_{\text{current}}} = J_{\text{current}}^{-1} \frac{\partial \mathbf{N}}{\partial \xi}$
(5)	ENDIF
(6)	<p>Compute the weight function presented in Eq. (28)</p> $a_{ij} = \frac{a_0(\ x_i - x_j\)}{\sum_{n=1}^{N_i^{GP}} w_n J_n a_0(\ x_i - x_n\)}$ <p>where</p> <ul style="list-style-type: none"> a_0 is the polynomial function defined in Eq. (29) w is the integration weight J is the jacobian N_i^{GP} is the number of the candidate gauss points within the internal radius of a sphere centered at point i
(7)	Evaluate the numerical nonlocal measure in Eq. (27) $\bar{E}_{\text{non},i}^k = \sum_{j=1}^{N_i^{GP}} w_j J_j a_{ij} \bar{E}_{s,j}^k$

determines the intensity of anisotropy of collagen fiber families. I_0 is a dimensionless parameter which determines the state of folding of fibers and, consequently, their mobilization.

It is noted that the secondary stiffening parameter, $I_0 = 1$ represents the case where fibers are not crimped even at the beginning of loading. The reason for this assumption lies in the type of examples employed in this study which are muscular tissues.

Appendix B presents the way the second Piola–Kirchhoff tensor and the corresponding elasticity tensor are derived. The following damage function is presented as

$$\tilde{G}(\bar{E}_t^k) = 1 - D_k = \begin{cases} 1 & \text{if } \bar{E}_t^k < \bar{E}_{\min} \\ \frac{\bar{E}_t^k - \bar{E}_t^k}{\bar{E}_{\max} - \bar{E}_{\min}} \exp \left[\left(\beta_k \frac{\bar{E}_t^k - \bar{E}_{\min}}{\bar{E}_{\min} - \bar{E}_{\max}} \right) \right] & \text{if } \bar{E}_{\min} \leq \bar{E}_t^k \leq \bar{E}_{\max} \\ 0 & \text{if } \bar{E}_t^k > \bar{E}_{\max} \end{cases} \quad (31)$$

Table 3
Material properties.

Material parameters	Values	Material parameters	Values
c_1 (MPa)	0.9	β_m	0.1
c_2 (MPa)	0	\bar{E}_{\min}^m ($\sqrt{\text{MPa}}$)	0.84
c_3 (MPa)	1.45	\bar{E}_{\max}^m ($\sqrt{\text{MPa}}$)	1.15
c_4	0.001	β_f	0.8
K (MPa)	2508.21	\bar{E}_{\min}^f ($\sqrt{\text{MPa}}$)	2.38
κ	0	\bar{E}_{\max}^f ($\sqrt{\text{MPa}}$)	3.9
I_0	1		

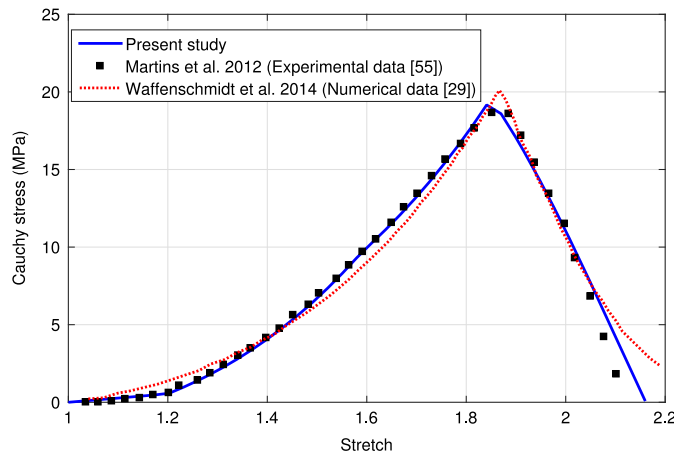


Fig. 3. Mechanical behavior of the abdominal rectus sheath.

where \bar{E}_{\max}^k and \bar{E}_{\min}^k are the total and initial equivalent strain parameters, respectively, and β_k is the exponential coefficient representing the damage saturation. This function reflects significant features of a robust potential in fitting data and the ability in better rate of convergence.

In the following, uniaxial tests are performed on samples of ligament and rectus sheath as the first and second examples. The third example is devoted to a perforated plate of the ligament subjected to stretch in order to investigate the mesh independency of the proposed damage model. A dog-bone sample of a hypothetical tissue is then analyzed to examine the mesh sensitivity and to study the differences between the proposed search-related updating algorithms. Finally, the roles of deformation and fiber alignment are investigated in a model, which resembles the aortic-dissection problem.

4.1. Uniaxial test: abdominal rectus sheath

The first numerical example is devoted to fitting capability of the damage function employed in this paper. This function is examined by the experimental data presented by Martins et al. [55] based on a sample from the muscular rectus sheath in abdomen, and is compared with the numerical simulation by Waffenschmidt et al. [29]. Material properties are presented in Table 3. Note that, owing to the muscular texture of the tissue, fibers are disposed in a parallel direction (Y direction in this example); hence, only one family of fiber with no fiber dispersion is assumed to capture the behavior. Consequently, a fully transversely isotropic case is obtained by setting the dispersion parameter κ equal to zero [29]. Fig. 3 represents variations of the true stress in a simple uniaxial experiment. Despite the drastic changes that appeared in the trend of experimental data in Fig. 3, the present damage model shows a more promising fitting on the overall trend and less relative errors than the reference numerical estimates.

Table 4
Material properties.

Material parameters	Values	Material parameters	Values
c_1 (MPa)	5.05	β_m	0.001
c_2 (MPa)	0	$\bar{E}_m^m (\sqrt{\text{MPa}})$	0.16353
c_3 (MPa)	46.0082	$\bar{E}_{\max}^m (\sqrt{\text{MPa}})$	0.2974
c_4	150.193	β_f	0.0001
K (MPa)	2508.21	$\bar{E}_{\min}^f (\sqrt{\text{MPa}})$	0.5
κ	0	$\bar{E}_{\max}^f (\sqrt{\text{MPa}})$	1.3342
I_0	1		

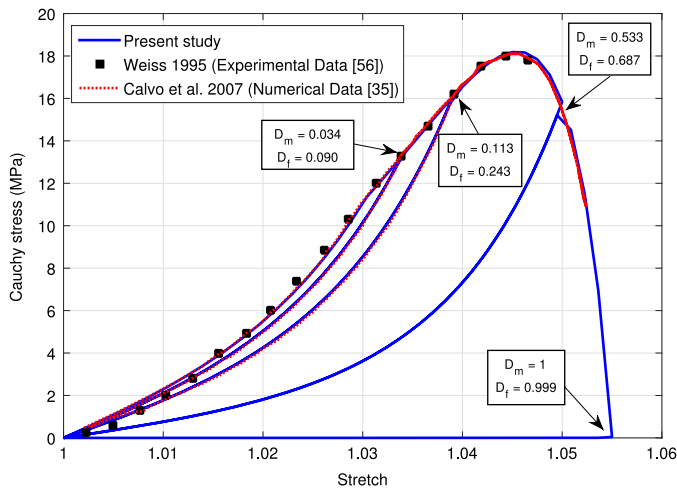


Fig. 4. Mechanical behavior of the ligament.

4.2. Uniaxial test: ligament

In the second example, the results of the employed damage function in a uniaxial tension experiment are compared with the one used by Calvo et al. [35] with material properties presented in Table 4. It is notable that one family of fiber is assumed for the ligament's simulation since the muscular texture of this tissue consists of parallel collagen fibers [35,56]. Fig. 4 illustrates the stress–stretch response of these simulations based on the experimental data presented by Weiss et al. [56]. Clearly, the current numerical model shows a precise agreement with the available reference experimental and numerical data.

4.3. Perforated plate

In this section, the popular example of a thin perforated square plate [3,29,35,36] is investigated exploiting the material parameters used in Calvo et al. [35] for the ligament simulation (Table 4). This example is aimed at demonstrating the mesh independency of the adopted integral type nonlocal model. Geometry, boundary conditions and four different meshes are presented in Fig. 5. Figs. 6 and 7 demonstrate the damage distribution in matrix and fiber at the end of loading for matrix and fibers, respectively. A precise agreement regarding the damage pattern and value is observed between the four distinct meshes, illustrating the capability of the proposed model to capture the damage pattern accurately and mesh independently. Furthermore, the global response is presented to show the overall behavior of the structure under specific boundary and loading conditions. Fig. 8 demonstrates a converging trend with refining meshes, which further illustrates the accuracy, mesh independency and robustness of the proposed approach.

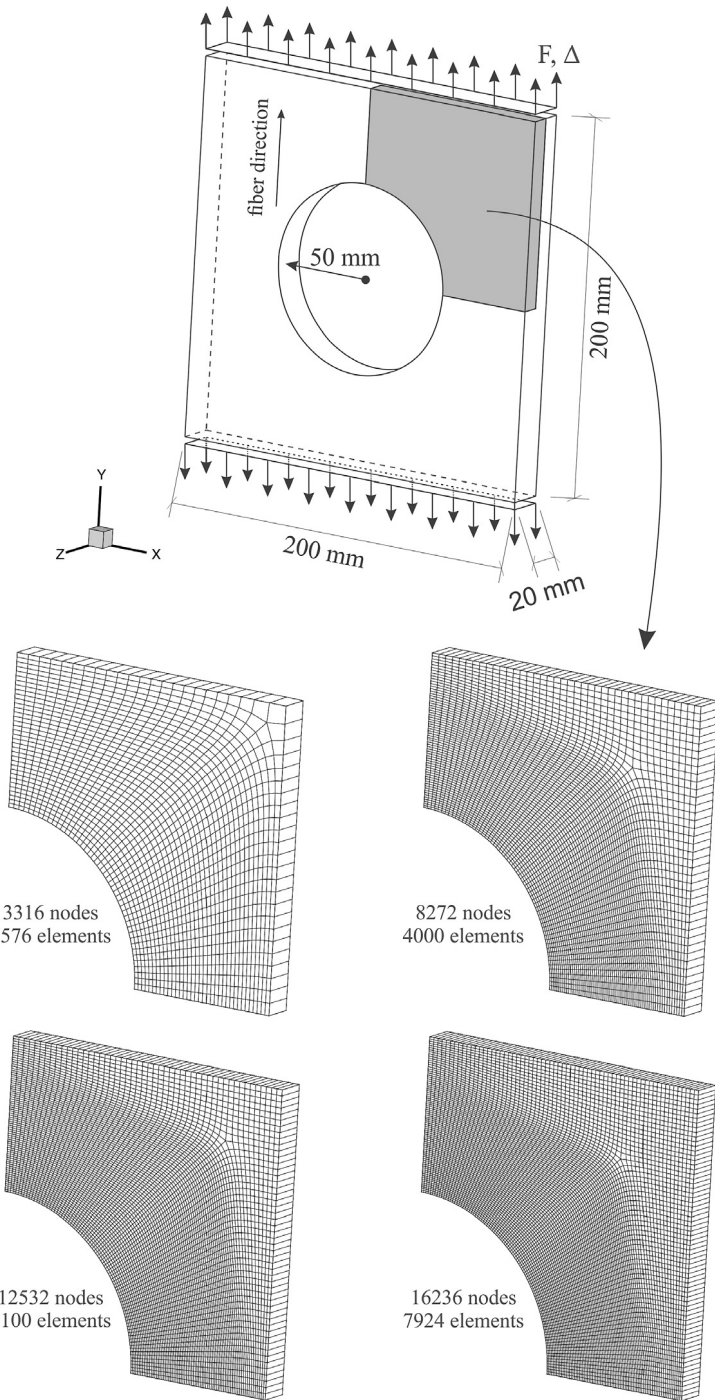


Fig. 5. Geometry, boundary conditions and four different meshes of the perforated plate.

Now, the effect of the characteristic length is investigated for a specific mesh. In order to perform a sensitivity analysis on the effect of integration radius on damage parameter, four different characteristic lengths are examined.

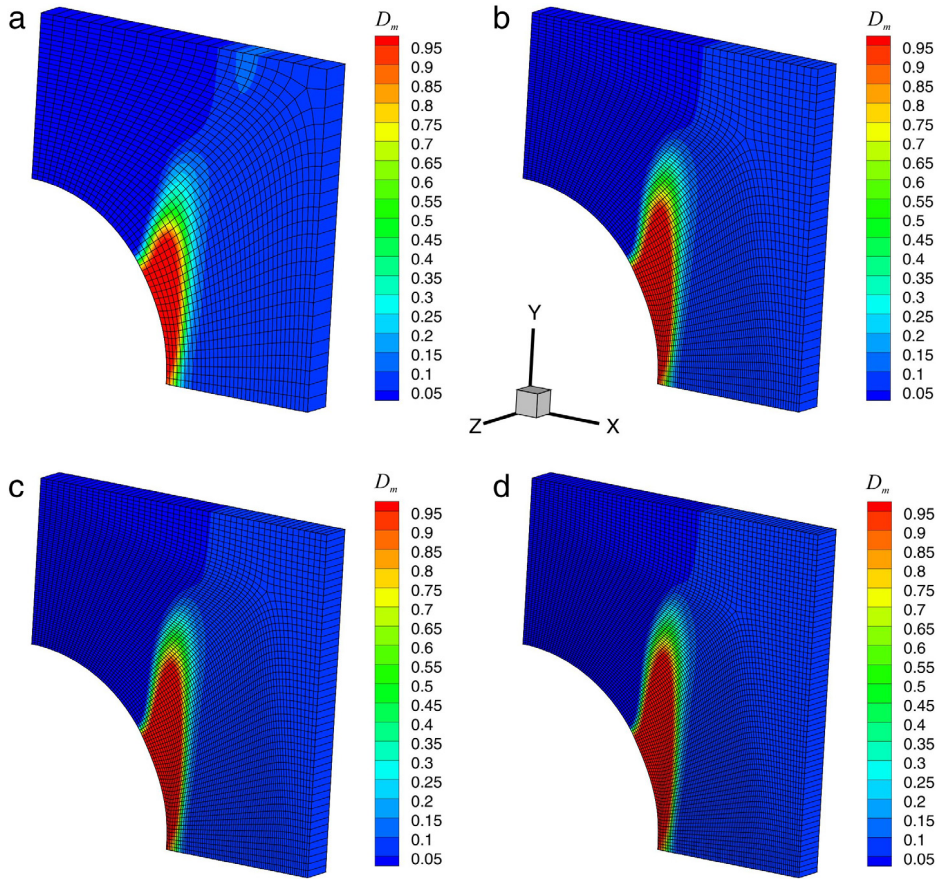


Fig. 6. Distribution of damage in matrix, (a) 1576 elements, (b) 4000 elements, (c) 6100 elements, (d) 7924 elements.

Figs. 9 and 10 illustrate the changes in damage parameter with alteration of the characteristic length. Fig. 9 shows a pure widening of the damage zone with the increase of the characteristic length. Similarly, Fig. 10 shows relatively different patterns with different values for D_f . The results obtained in the present study cannot be conclusively used to determine how increasing the characteristic length or the number of integration points may generally affect the final trend of solution, which requires further independent investigation.

4.4. Dog bone sample

In this example, a dog-bone shaped sample of a hypothetical tissue is investigated to analyze the mesh independency and, to assess the three algorithms presented in Table 2 for updating the non-local formation. Geometry and material properties are presented in Fig. 11 and Table 5, respectively. Once more, three distinct meshes are investigated to study the mesh independency of the employed damage model (see Fig. 11). Note that, the number of elements in these meshes is deliberately chosen with substantial differences in order to better capture possible changes, if any. Figs. 12 and 13 demonstrate the damage distribution for matrix and fibers, respectively. A slight discrepancy in the damage zone is observed between the first mesh and the rest. The reason lies within the relatively coarse size of the first mesh. In general, however, results for all meshes, specially the two fine meshes, are very similar and acceptable.

Fig. 14 shows the global response of these three meshes, and the good convergence performance with mesh refinement (see the focused zone in Fig. 14).

To address the proper updating algorithm for soft tissue problems which undergo large deformations, the algorithms based on Table 2 are implemented for one mesh (2136 elements). As discussed before, while the first algorithm

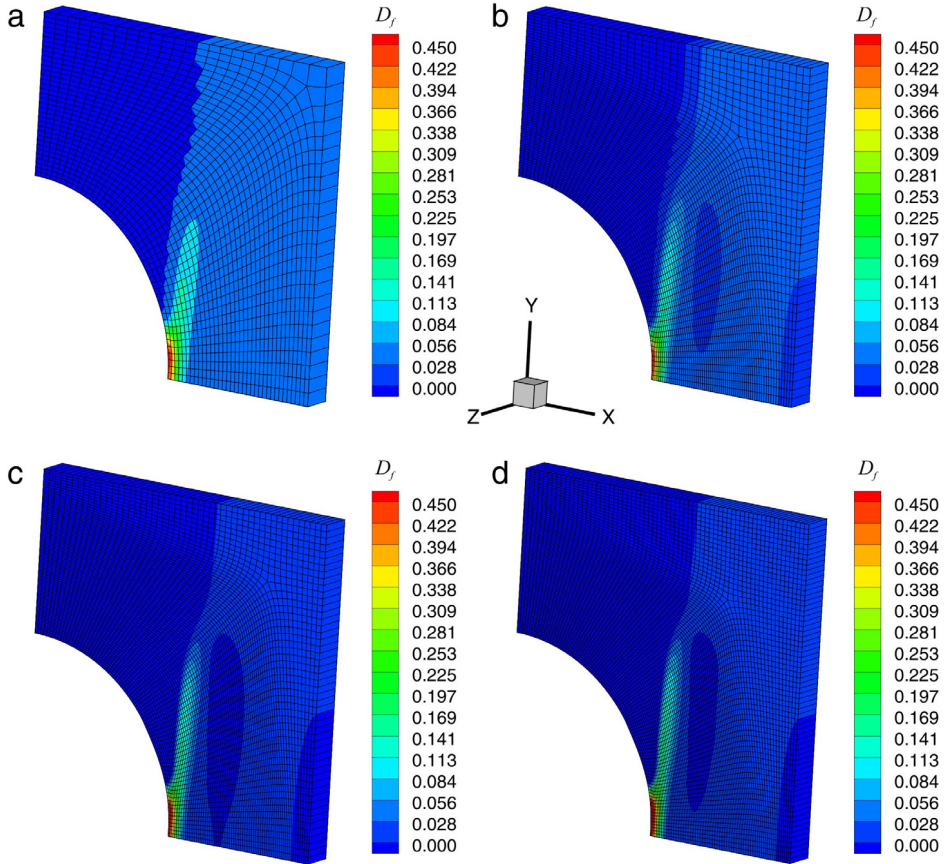


Fig. 7. Distribution of damage in fiber, (a) 1576 elements, (b) 4000 elements, (c) 6100 elements, (d) 7924 elements.

Table 5
Material parameters.

Material parameters	Values	Material parameters	Values
c_1 (MPa)	1	β_m	1
c_2 (MPa)	0	$\overline{E}_{\min}^m (\sqrt{\text{MPa}})$	0.335749
c_3 (MPa)	20	$\overline{E}_{\max}^m (\sqrt{\text{MPa}})$	1.5
c_4	3.54	β_f	1
K (MPa)	2508.21	$\overline{E}_{\min}^f (\sqrt{\text{MPa}})$	0.7
κ	0	$\overline{E}_{\max}^f (\sqrt{\text{MPa}})$	5
I_0	1		

is the general integral type nonlocal formulation, which performs well in small strain problems, the second and third approaches are required for updating the location of Gaussian points and searching for the candidate points, respectively, in very large deformation regimes.

The two identical contours in Figs. 15 and 16 (labeled by b and c) are associated with the second and third algorithms. Based on these observations, while under rather small stretches, the effect of search update is not important, updating the location of the Gaussian points has some effects on the damage orientation and value, with

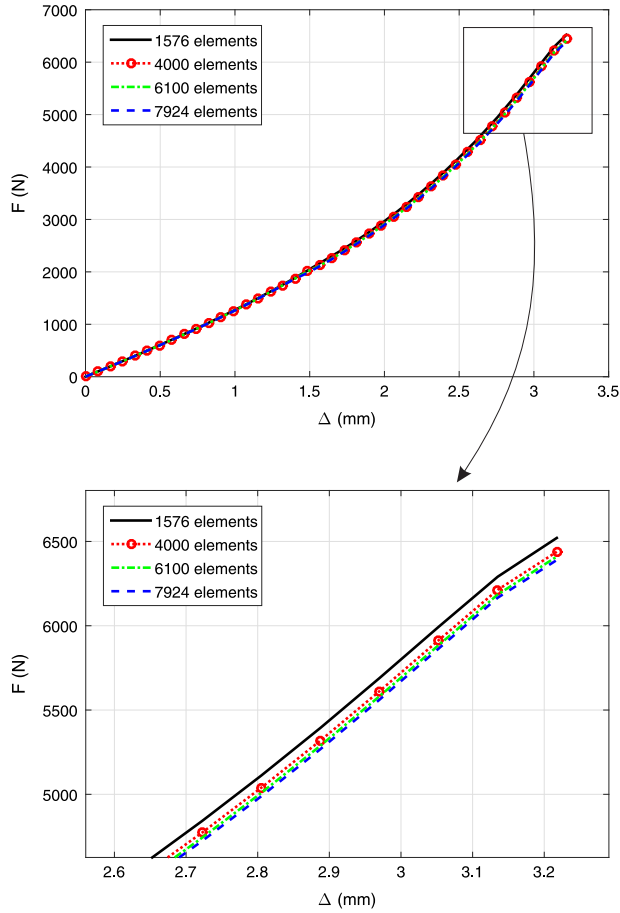


Fig. 8. Global response of the perforated plate.

approximately 7% discrepancy in the damage values, as observed in Fig. 16. It should be noted that while small stretches cannot genuinely reveal the need for search updates, a more complex loading state, such as out of plane deformation or biaxial-shear loading combination, may disclose the differences among the second and third algorithms more clearly, as it will be investigated in the last example (Section 4.5).

4.5. Role of fibers in tearing phenomenon

Aorta, as a biological composite, consists of three layers, intima, media and adventitia [57]. Aortic dissection is a fatal disease which annually affects at least 30 cases out of a million individuals [58]. Upon initiation with an intimal tear in intima, the aortic dissection propagates through the sub-adventitial plane, i.e. either between the sub-layers of the media or between the media and adventitia [58,59]. This disease often occurs in people with history of high blood pressure, and causes rupture in aorta and decrease in blood supply of other organs; leading to immediate death. Several works in the literature are dedicated to this disease by incorporating a cohesive crack model for simulation of rupture [57,59,60].

This example is dedicated to the indispensable role of fibers in damage propagation in media layer of aorta. This simulation, known as the peeling test, is a slow and controllable form of the medial dissection [61]. The purpose of the peeling experiment is to investigate the fracture and failure properties of aortic dissection. Due to the experience of

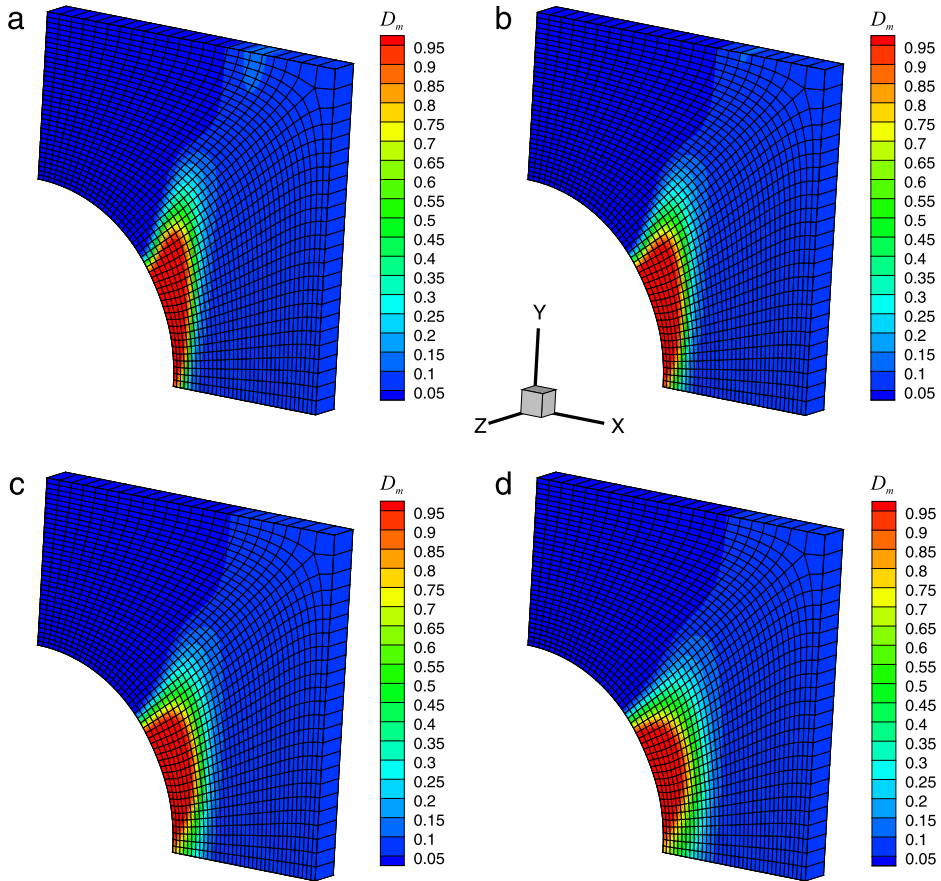


Fig. 9. The effect of the characteristic length on damage of matrix, (a) $R = 0.006$ mm, (b) $R = 0.01$ mm, (c) $R = 0.015$ mm, (d) $R = 0.02$ mm.

large deformation in soft tissues, orientation of fibers changes drastically, which substantially affects the total response of the soft tissue.

In this study, based on the peeling experiments performed by Sommer et al. [61], tearing of media is investigated using the damage model (30). Despite the fact that many works in literature have investigated the mechanical response of the aorta media [34,41], none of these works, however, have considered the softening behavior of this layer.

The lack of experimental data on the softening behavior of media has limited the precise simulation of aortic dissection to determine damage commencement and completion. Table 6 shows material parameters exploited in this example. Histological and intact material parameters are adopted from the work by Gasser and Holzapfel [59], whereas damaged ones are assumed based on an engineering sense which stems from the preceding examples. The parameter θ is the angle between each family of fiber and the axis parallel to the length of the sample (X direction).

Similar to previous examples, mesh dependency is explored by two different meshes. Geometry, boundary condition and meshes are illustrated in Fig. 17. Rotation of fibers with respect to the loading direction can profoundly affect the rupture propagation state.

Global force-displacement responses of the medial dissection model for two different meshes and three different algorithms are demonstrated in Fig. 18, which shows insensitivity of analysis to the adopted finite element meshes. Moreover, no difference is observed for the *updated distance* and *updated distance and search* algorithms within the rather small stretches ($\Delta = 0.5$ mm). This similarity between the results of these two algorithms is also seen in the dog-bone sample (see Figs. 15 and 16). However, a remarkable difference is observed at the very first steps of loading

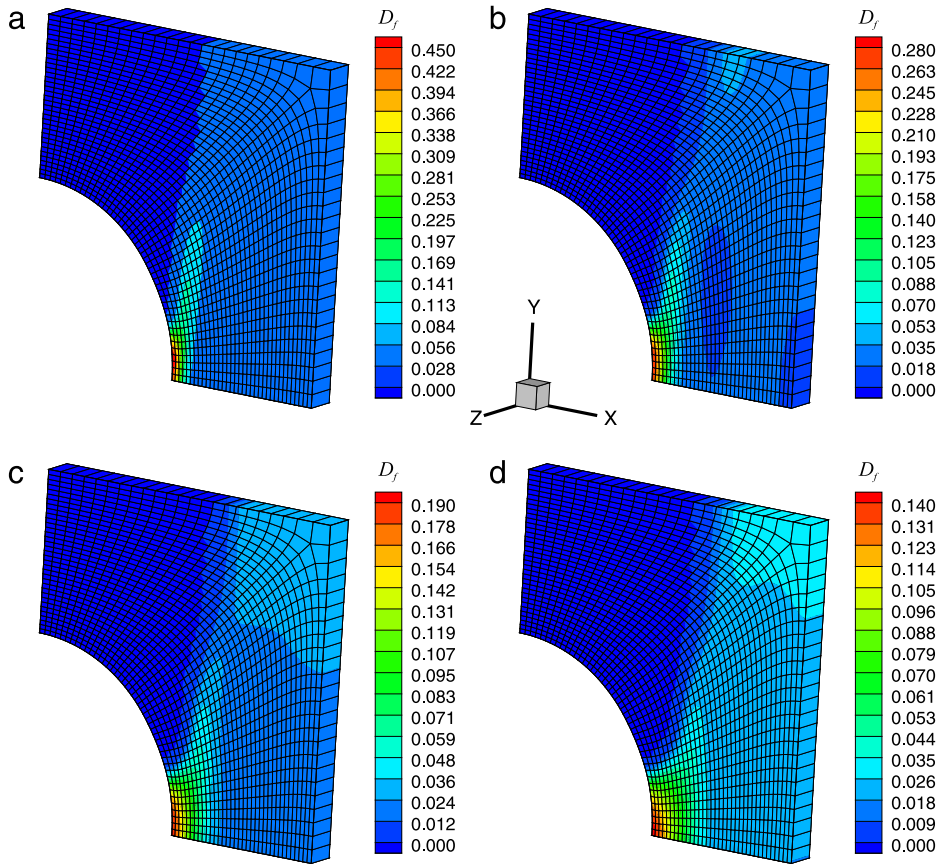


Fig. 10. The effect of the characteristic length on damage of fiber, (a) $R = 0.006$ mm, (b) $R = 0.01$ mm, (c) $R = 0.015$ mm, (d) $R = 0.02$ mm.

Table 6
Material parameters.

Material parameters	Values	Material parameters	Values
c_1 (kPa)	16.2	β_m	0.1
c_2 (kPa)	0	$\bar{E}_{\min}^m (\sqrt{\text{kPa}})$	1.2
c_3 (kPa)	98.1	$\bar{E}_{\max}^m (\sqrt{\text{kPa}})$	9
c_4	10	β_f	0.1
K (kPa)	2508.21	$\bar{E}_{\min}^f (\sqrt{\text{kPa}})$	1.5
κ	0	$\bar{E}_{\max}^f (\sqrt{\text{kPa}})$	25
I_0	1	θ (deg)	5

($\Delta = 0.2$ mm) in the *no update* algorithm, (see Fig. 18), which shows the incompetence of the *no update* algorithm in solving this problem.

Since the aortic dissection problem deals with a combination of shear and normal loadings, the search update procedure may substantially change the global response and damage distribution in larger stretches ($\Delta > 0.5$ mm).

In order to further elaborate existing differences in Fig. 18, contours of damage in both fiber and matrix for three different loading steps (stages A, B and C) are examined, as presented in Fig. 19. It is clearly observed that both damages in matrix and fiber can substantially affect the global response. On the other hand, the global response is directly affected from the loading edge (see Fig. 17), which itself is influenced by the occurrence of damage.

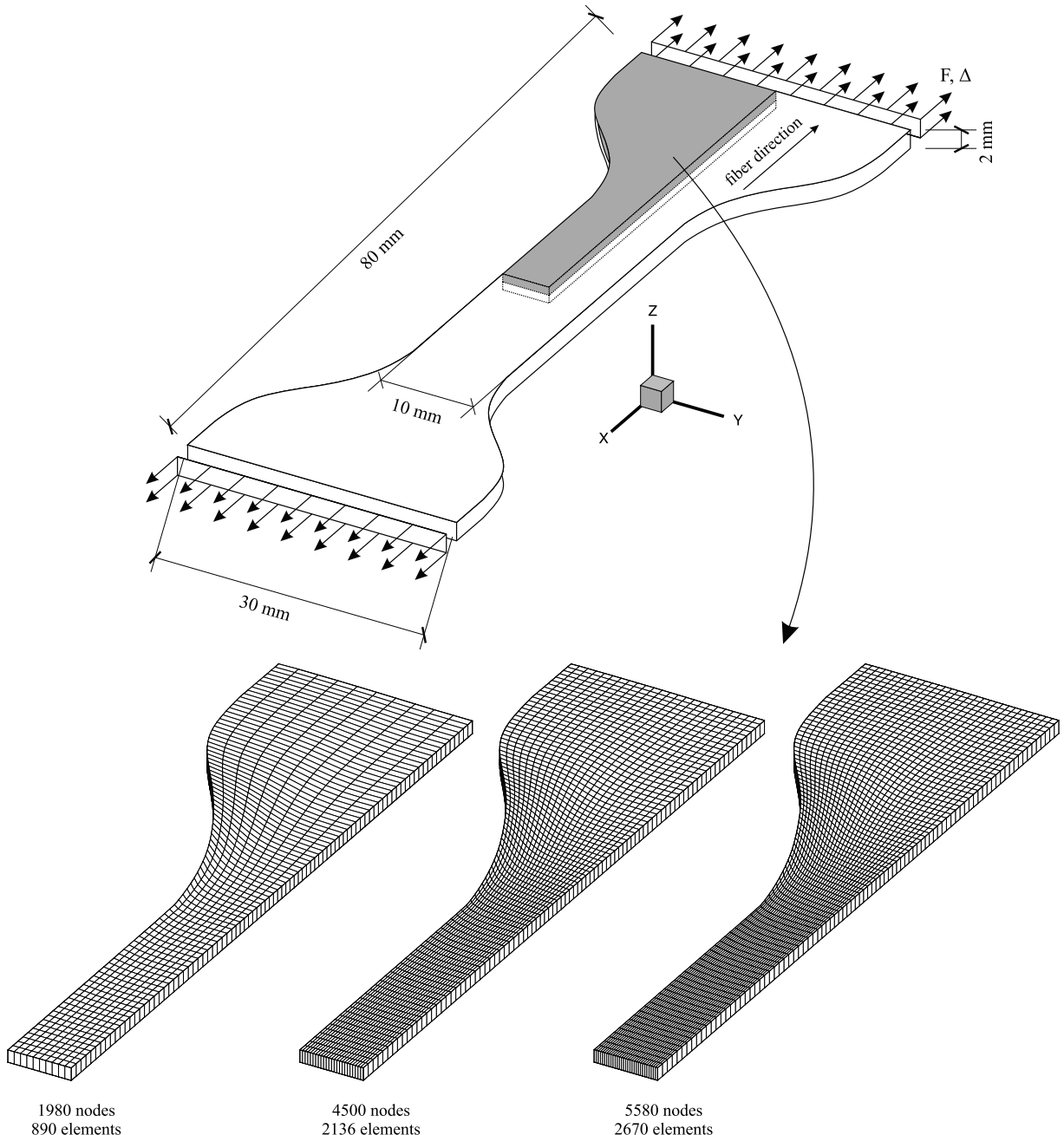


Fig. 11. Geometry, boundary conditions and four different meshes of the dog bone sample.

In the stage A, which is in the initial steps of loading, no apparent damage is observed in fibers, while the damage occurs only in matrix. Hence, the damage in matrix rules the global response. Since the damage value in the *no update* algorithm is more severe than the other two (with more or less equal damaged zones), predictions of this algorithm become lower than the other two.

In the second stage of loading (stage B), however, both fiber and matrix crucially contribute in the global response. It is observed that the *no update* algorithm predicts higher levels of damage in matrix and fiber than the two other algorithms, specially on the loading edge. As a result, predictions of this algorithm remain well lower than the other two (see Fig. 18).

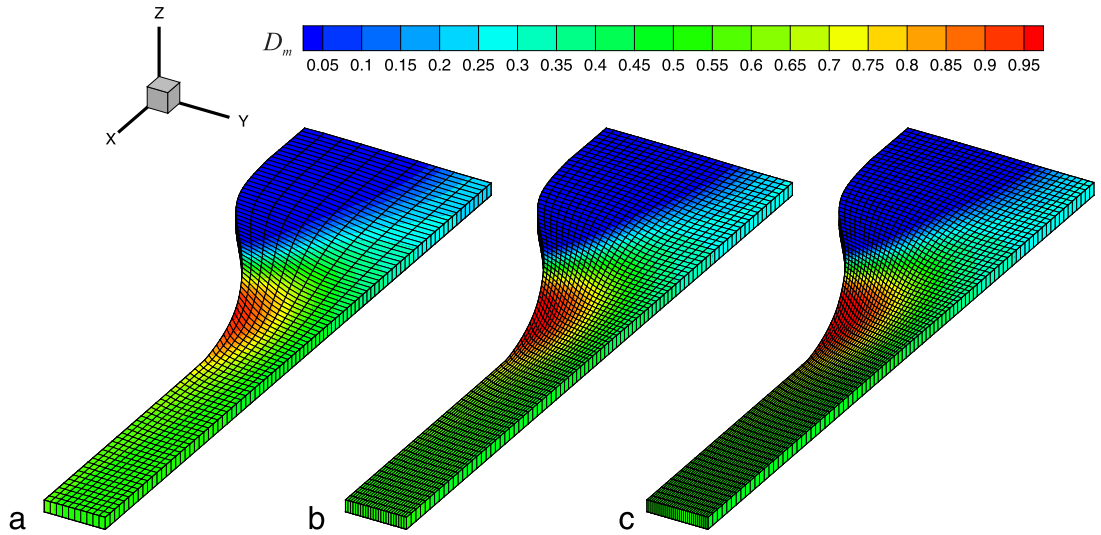


Fig. 12. Distribution of damage in matrix, (a) 890 elements, (b) 2136 elements, (c) 2670 elements.

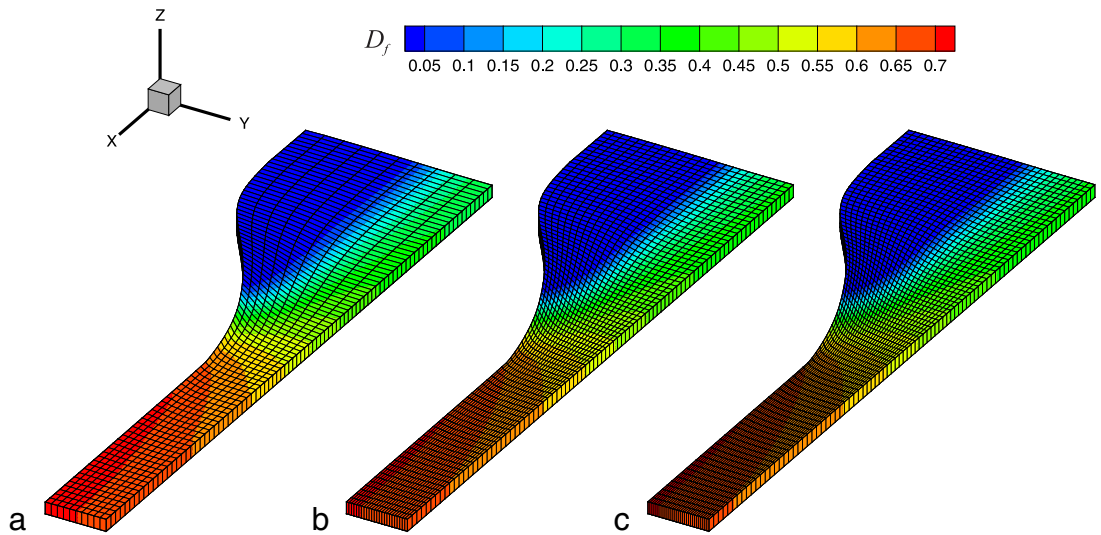


Fig. 13. Distribution of damage in fiber, (a) 890 elements, (b) 2136 elements, (c) 2670 elements.

Now, focusing on the second and third columns of Fig. 19 for stage B, it is evident that fibers remain almost intact in both *updated distance* and *updated distance and search* algorithms. Nevertheless, higher damage of matrix predicted by the *updated distance and search* algorithm than the *updated distance* procedure leads to its lower global response at this stage.

In stage C, and similar to previous stage, the *no update* algorithm illustrates a wider zone of matrix and fiber damage near the tearing zone and the loading edge compared with the two other algorithms. Although the matrix damage seems to be a little wider in the *updated distance* than the *updated distance and search* algorithm, the *updated distance and search* algorithm predicts substantially lower values for the fiber damage, with an almost intact loading edge. Such a strength reduction in the leading component (fiber) of load bearing capacity results in a lower global response predicted by the *updated distance* algorithm than the one anticipated by *updated distance and search* algorithm, as anticipated in Fig. 18.

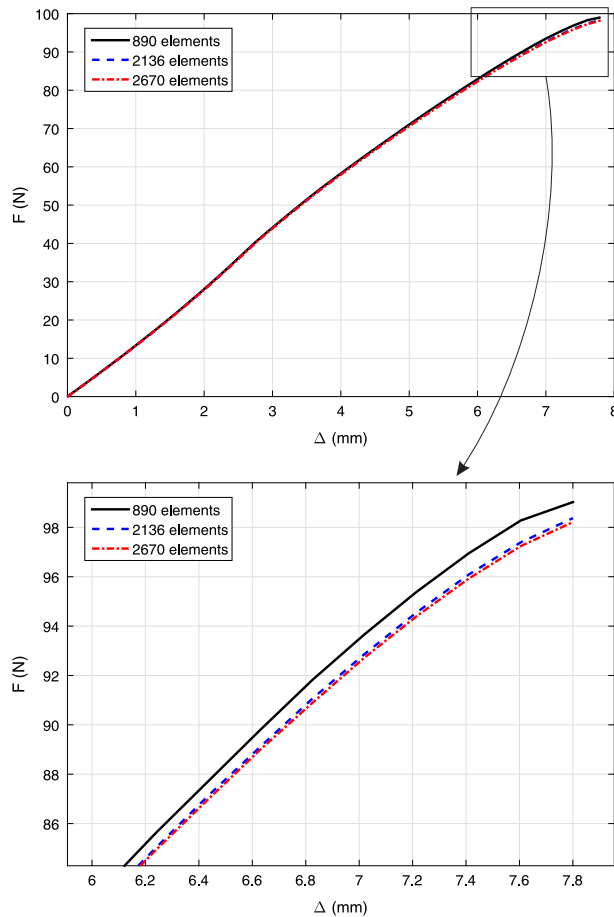


Fig. 14. Global response of the dog bone sample.

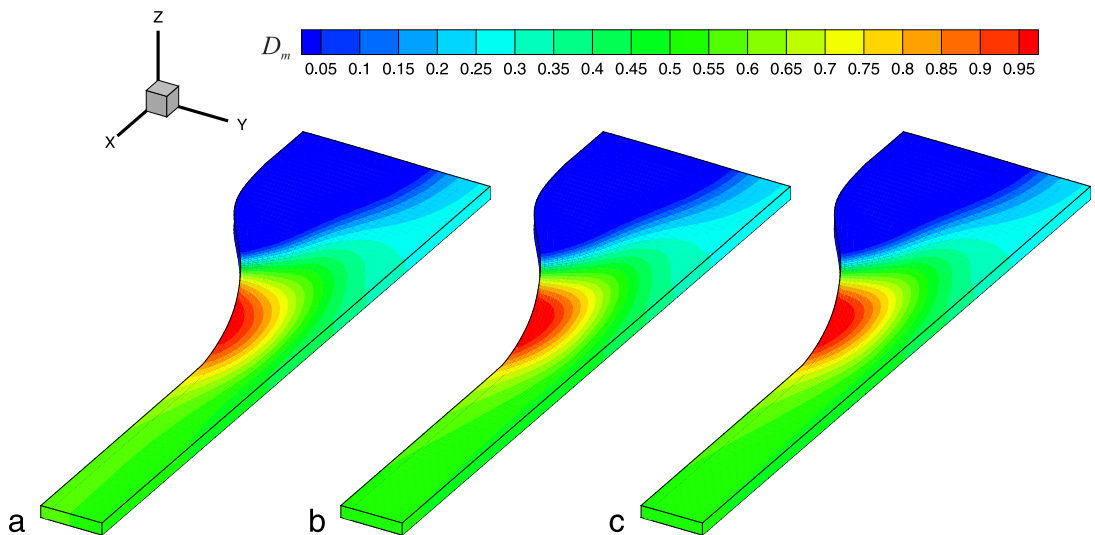


Fig. 15. Effect of the updating algorithm on damage of matrix, (a) no update algorithm, (b) updated distance algorithm, (c) updated distance and search algorithm.

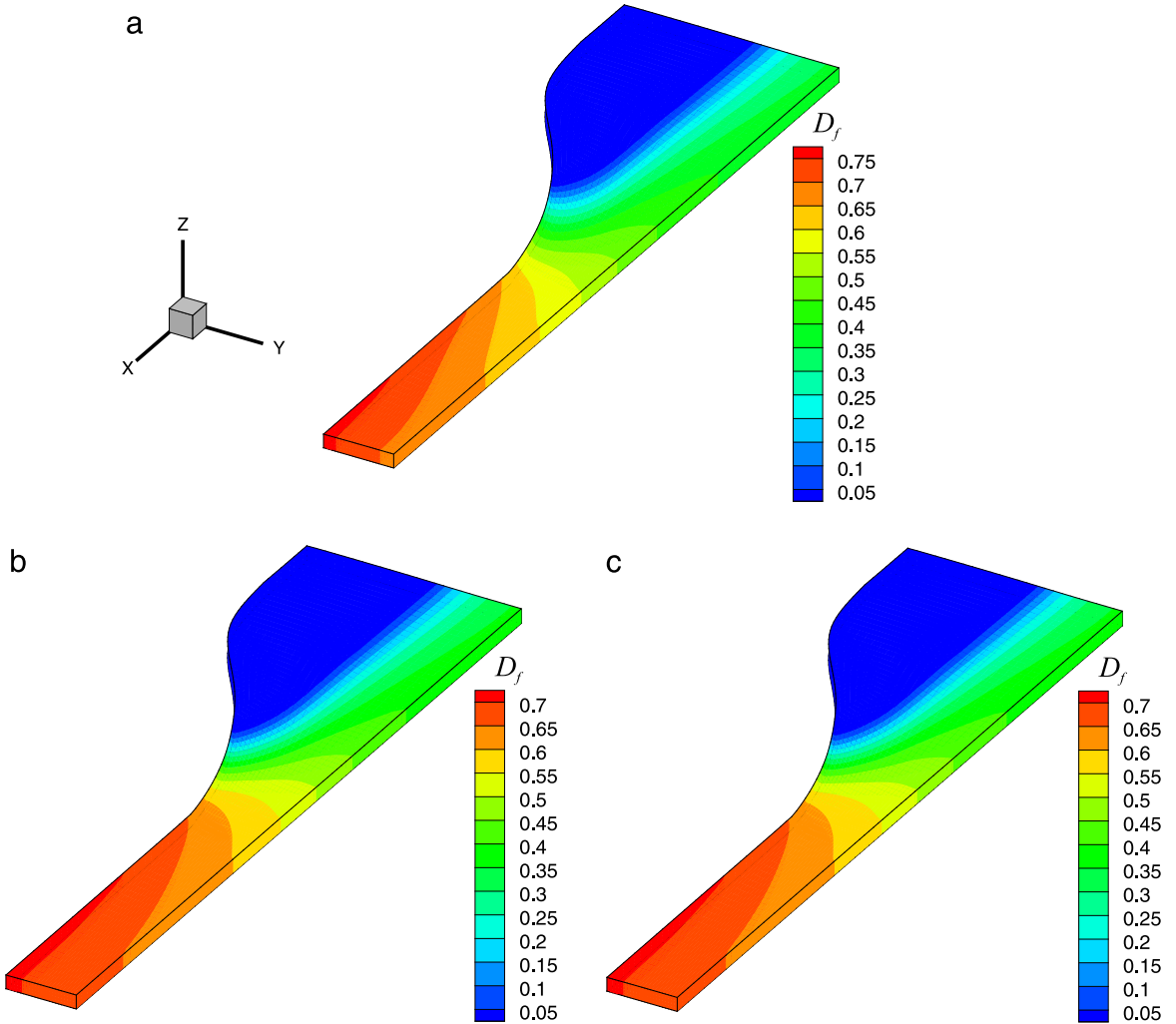


Fig. 16. Effect of the updating algorithm on damage of fiber, (a) *no update* algorithm, (b) *updated distance* algorithm, (c) *updated distance and search* algorithm.

Based on the *updated distance and search* algorithm, damage contours of the matrix and the first family of fibers on two different meshes are presented in Figs. 20 and 21. It is clearly observed that the results remain mesh independent. It should be noted that contours of the second family are mirrors of the presented contours since the problem is symmetric with respect to the XZ plane.

Furthermore, the lack of experimental data on the softening behavior of medium has limited the precise simulation of aortic dissection to determine damage commencement and completion; otherwise, a comparison between the experimental data and numerical predictions could be performed. Nevertheless, the use of *updated distance and search* algorithm seems more logical in cases where large deformation and rotation may cause candidate gauss points to disperse, and so a new search may be required. This choice remains an open question for further investigation.

According to Fig. 20, damage in the gel-like material initiates from the location where both the shear and normal stress components govern the damage state. Existence of anisotropy due to the fiber dispersion complicates the solution. To reveal the cause of complex behavior of fiber damage in Fig. 21, a precise measure of fibers local orientation is explored in Figs. 22 and 23. Based on the level of deformation of elongated fibers and the damage threshold, three different conditions are distinguished for the behavior of fibers. The blue color determines the

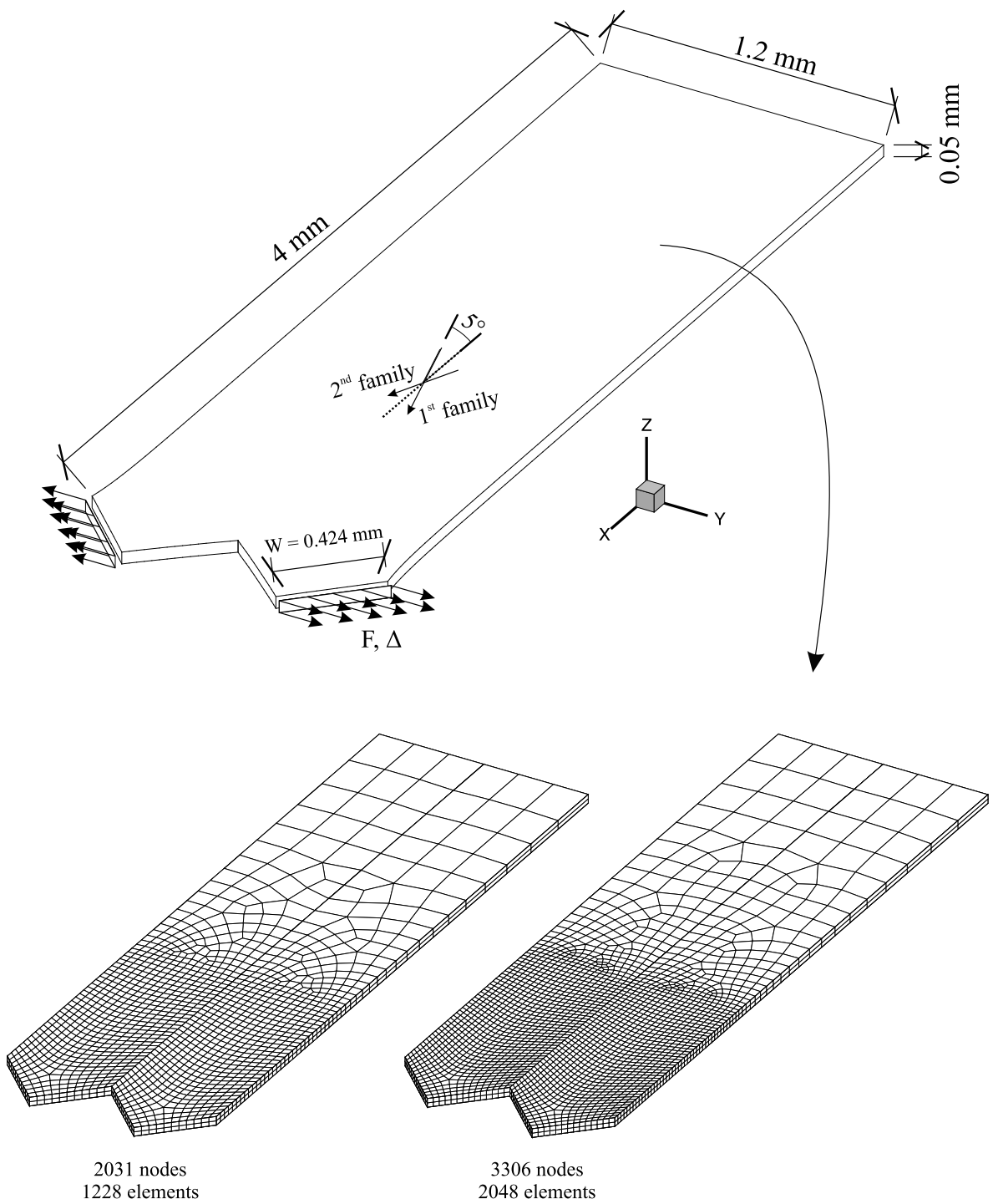


Fig. 17. Geometry, boundary conditions and two different meshes of the medial dissection.

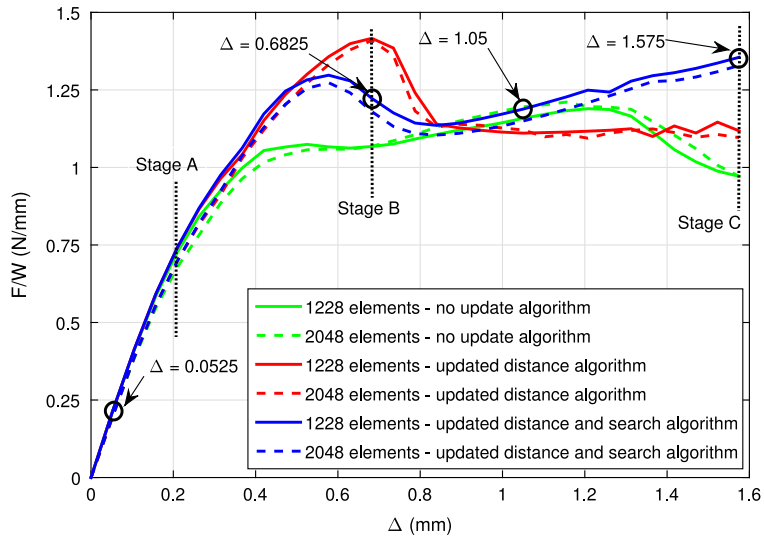


Fig. 18. Global response of the medial dissection; green lines are devoted to the *no update* algorithm; red lines are devoted to the *updated distance* algorithm; blue lines are devoted to the *updated distance and search* algorithm. (For interpretation of the references to color in this figure legend, the reader is referred to the web version of this article.)

shortened fibers which do not contribute in load bearing anymore; they are *inactive*. Some fibers, illustrated by the green color, are elongated but they have not reached the initial threshold for damage; hence, they remain *active*. Some other fibers are *damaged*, and are colored by red. Not only are they elongated, but also they have passed the threshold value of damage.

Figs. 22 and 23 show the predicted local orientations of the first and the second family of fibers based on the *updated distance and search* algorithm in different steps of loading. Local alteration of fiber orientation and various states of inactive, active and damaged fibers are comprehensively illustrated. It should be noted that although some fibers are aligned along the direction of loading (see the magnified zones in Fig. 23), they cannot bear loads because they are shortened and *inactive* (see the blue vectors). Illustration of vectors and their associated mobilization conditions in Figs. 22 and 23 can help explain the distribution of fibers damage in Fig. 21.

5. Conclusion

An integral-type nonlocal scheme was incorporated to circumvent the problem of mesh dependency and spurious localization in soft fiber-reinforced tissues. A comprehensive formulation pertaining to continuum damage for hyperelastic materials was presented by introducing a new form of a damage function showing robust capability in fitting and convergence. Taking into account large deformations, three different algorithms regarding the proposed nonlocal method were investigated. Despite the fact that the distance updating was adequate for the direct stretch problem, updating both the distance and search for candidate gauss points would seem to be more logical in cases where large deformations and rotations occur. Nevertheless, the choice of the updating scheme would remain an open question for further investigation.

It should also be noted that the way mesh refinement was performed and the local size of elements played an important role in obtaining the results, as they directly affected the number of gauss points participating in a fixed radius of integration in an integral-type nonlocal method.

Also, the inevitable role of fibers, as the most load bearing component of soft tissues, was comprehensively examined. Large rotations could locally change the position/direction of some fibers, which would be crucial in the overall mechanical response of the tissue, as presented in the last example.

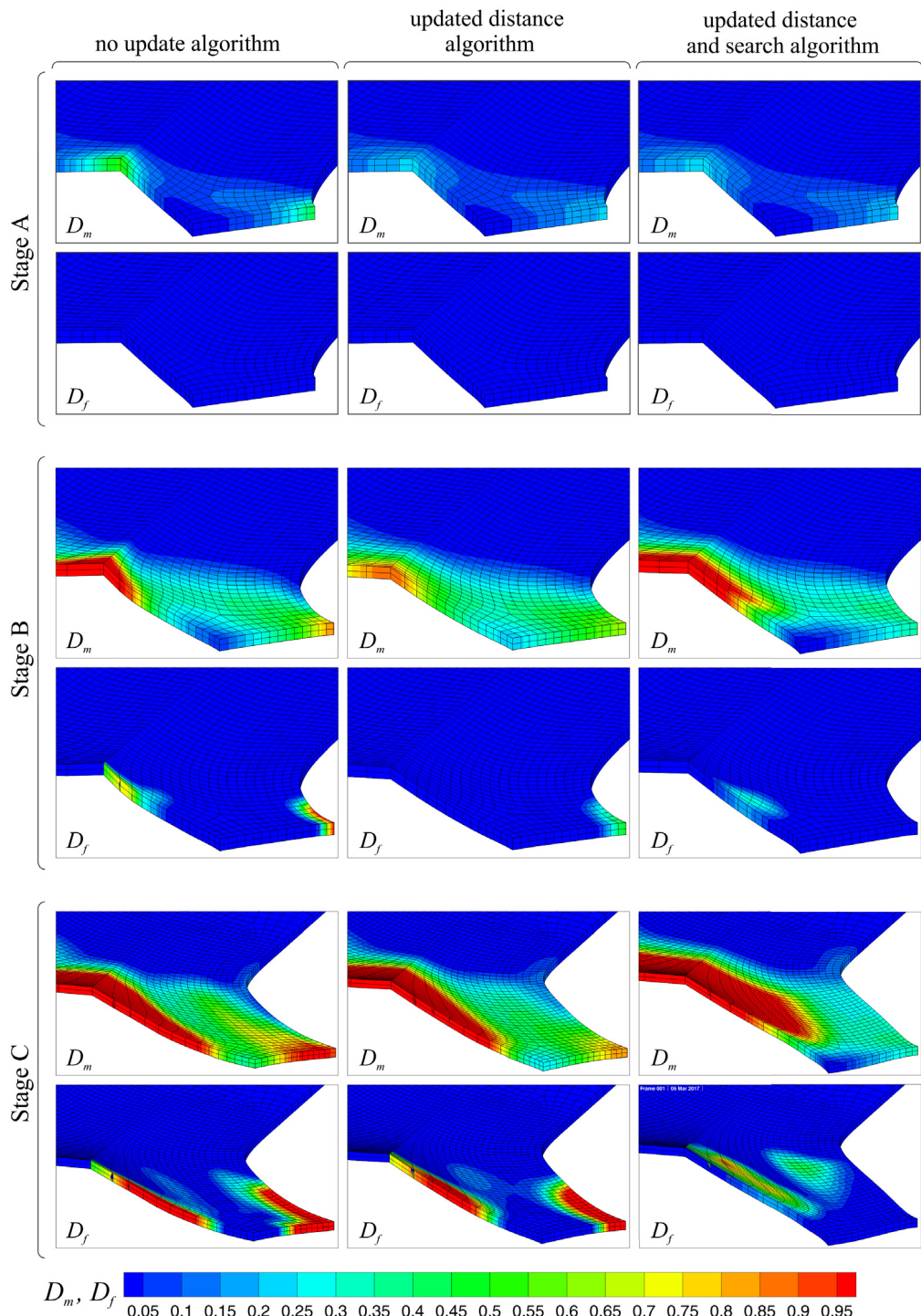


Fig. 19. Damage contours of matrix and the first family of fibers for the fine mesh (2048 elements). Columns from left to right: *no update algorithm*, *updated distance algorithm* and *updated distance and search algorithm*.

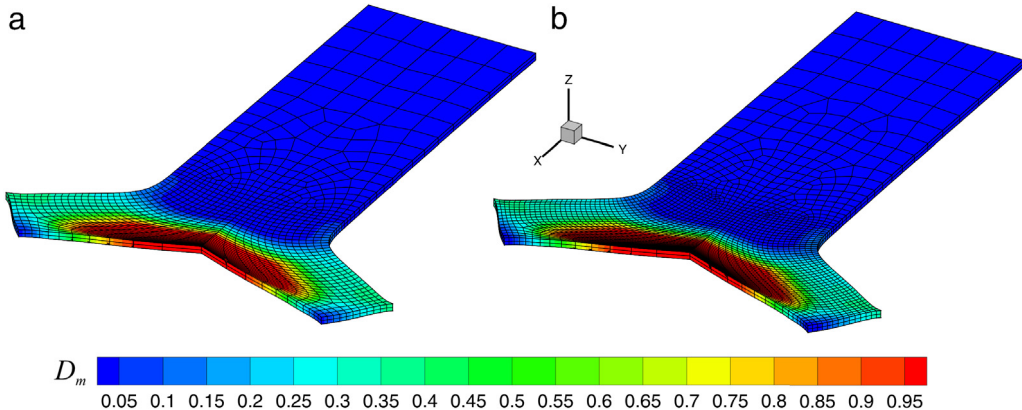


Fig. 20. Distribution of damage in matrix for *updated distance and search* algorithm, (a) 1228 elements and (b) 2048 elements.

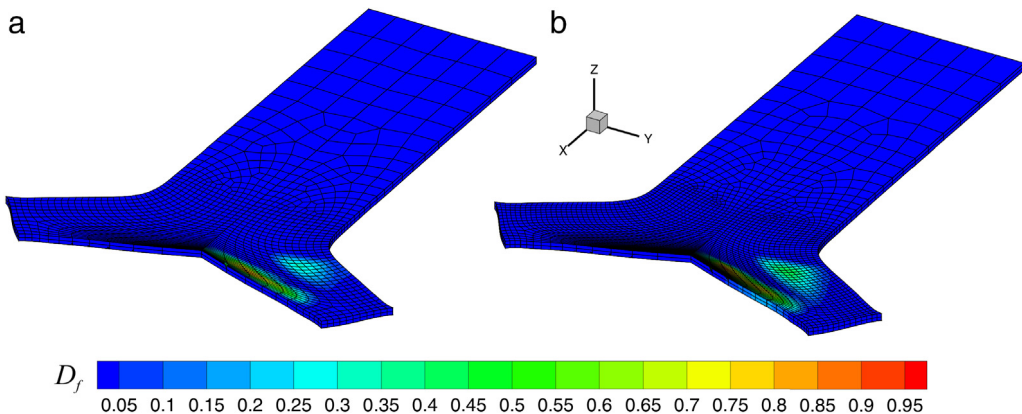


Fig. 21. Distribution of damage in the first family of fibers for *updated distance and search* algorithm, (a) 1228 elements and (b) 2048 elements. (For interpretation of the references to color in this figure legend, the reader is referred to the web version of this article.)

The present work can be further enhanced by combining the existing continuum damage formulation with the powerful capabilities of meshless methods or the extended finite element method (XFEM) to allow for capturing the tearing phenomena in soft biological tissues.

Acknowledgments

The authors wish to acknowledge the technical support of the High Performance Computing Lab, School of Civil Engineering, University of Tehran. The financial support of Iran National Science Foundation (INSF) is gratefully acknowledged.

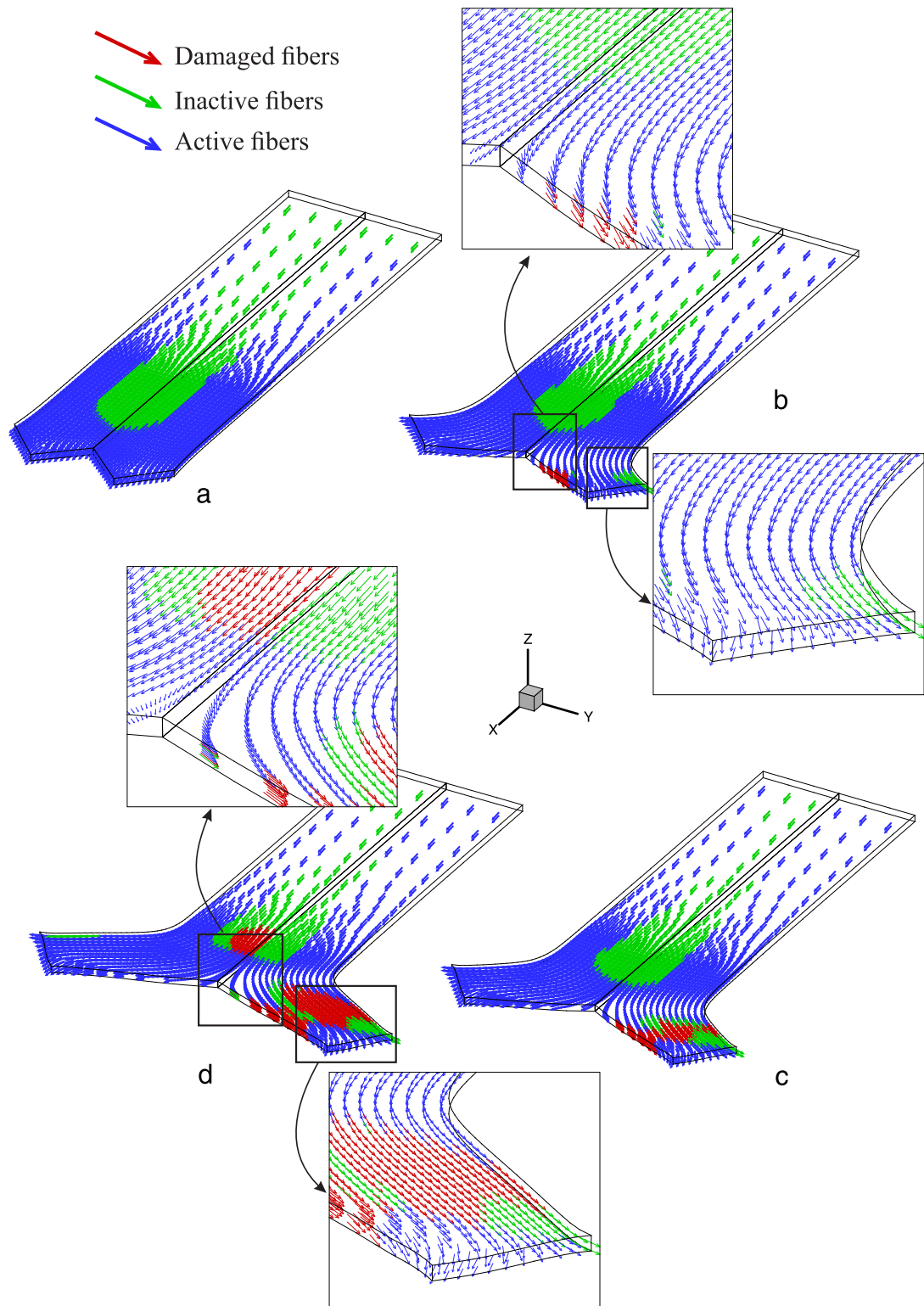


Fig. 22. Local reorientation of the first family of fibers in different loading steps for *updated distance and search* algorithm, (a) $\Delta = 0.525 \text{ mm}$, (b) $\Delta = 0.6825 \text{ mm}$, (c) $\Delta = 1.05 \text{ mm}$, (d) $\Delta = 1.575 \text{ mm}$. (For interpretation of the references to color in this figure legend, the reader is referred to the web version of this article.)

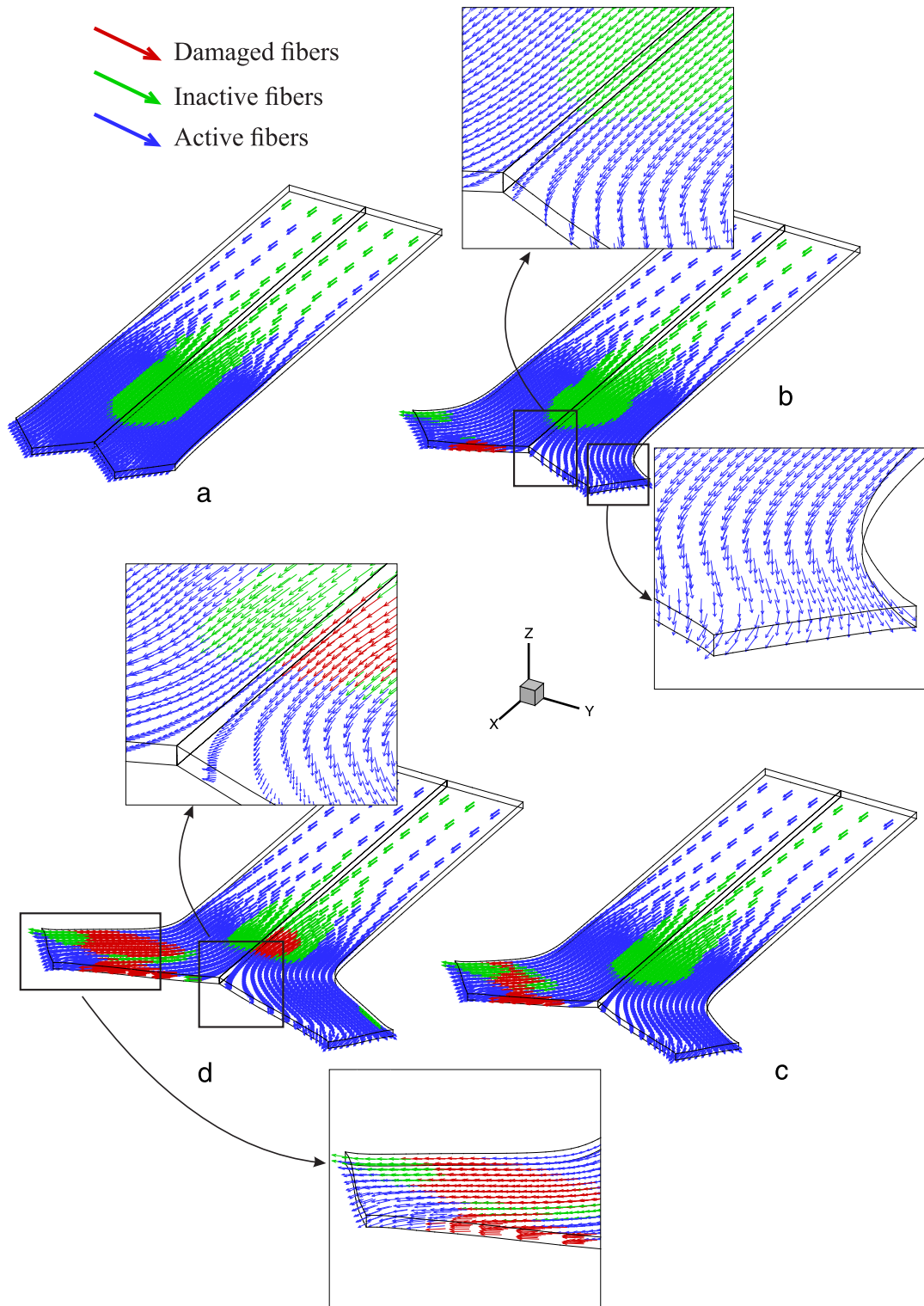


Fig. 23. Local reorientation of the second family of fibers in different loading steps for *updated distance and search* algorithm, (a) $\Delta = 0.525 \text{ mm}$, (b) $\Delta = 0.6825 \text{ mm}$, (c) $\Delta = 1.05 \text{ mm}$, (d) $\Delta = 1.575 \text{ mm}$. (For interpretation of the references to color in this figure legend, the reader is referred to the web version of this article.)

Appendix A. Finite element discretization

This appendix presents the finite element implementation of governing equations, and the details of exploiting the proposed updating procedures. Eight noded (brick) elements with eight Gaussian points are employed. Exploiting the isoparametric finite element approximation in the material description, the geometry \mathbf{X} can be interpolated by the shape functions \mathbf{N}_a [45],

$$\mathbf{X} = \sum_{a=1}^{N_{node}} \mathbf{N}_a (\varsigma_1, \varsigma_2, \varsigma_3) \mathbf{X}_a \quad (\text{A.1})$$

where N_{node} is the number of nodes per element. Furthermore, ς_1 , ς_2 and ς_3 are the reference coordinates, and \mathbf{X}_a represents the nodal measures. The displacement \mathbf{u} can be similarly interpolated as [45],

$$\mathbf{u} = \sum_{a=1}^{N_{node}} \mathbf{N}_a (\varsigma_1, \varsigma_2, \varsigma_3) \mathbf{u}_a. \quad (\text{A.2})$$

Interpolation of the deformation gradient of a point within an element can be expressed by,

$$\mathbf{F} = \sum_{a=1}^n x_a \otimes \nabla_0 N_a, \quad F_{iI} = \delta_{iI} + \sum_{j=1}^{N_{node}} \frac{\partial N_j}{\partial X_I} u_{ij} \quad (\text{A.3})$$

where ∇_0 is the gradient operator corresponding to the initial coordinates, and N_{node} is the number of nodes.

Discretization of the equilibrium equation based on the total and updated lagrangian formulations is now briefly presented [45].

A.1. Total lagrangian formulation

The linearized total lagrangian weak form equation is written as [45],

$$\int_V \delta \mathbf{E} [\delta \mathbf{u}] : \mathcal{C} : \mathbf{E} [\mathbf{u}] dV + \int_V \mathbf{S} : [(\nabla_0 \mathbf{u})^T \nabla_0 \delta \mathbf{u}] dV = \int_{\partial V} \mathbf{t}_0 \cdot \delta \mathbf{u} dA + \int_V \mathbf{b}_0 \cdot \delta \mathbf{u} dV \quad (\text{A.4})$$

where the subscript 0 denotes the material description, and $\delta \mathbf{u}$ is an arbitrary virtual deformation. The final well-known matrix form is written as [44],

$$\begin{aligned} & (\mathbf{K}_L + \mathbf{K}_{NL}) \mathbf{u} = \mathbf{R} - \mathbf{R}_i, \\ & \mathbf{K}_L = \int_V \mathbf{B}_L^T \hat{\mathbf{C}} B_L dV, \\ & \mathbf{K}_{NL} = \int_V \mathbf{B}_{NL}^T \hat{\mathbf{S}} B_{NL} dV, \\ & \mathbf{R} = \int_{\partial V} \mathbf{t}_0 \cdot \delta \mathbf{u} dA + \int_V \mathbf{b}_0 \cdot \delta \mathbf{u} dV, \\ & \mathbf{R}_i = \int_V \mathbf{B}_L \hat{\mathbf{S}} dV, \end{aligned} \quad (\text{A.5})$$

where $\hat{\mathbf{C}}$ is the 6×6 elastic matrix deduced from the minor and the major symmetry of the fourth order elastic tensor \mathcal{C} , and $\hat{\mathbf{S}}$ is a 9×9 transformed matrix of the symmetric second Piola–Kirchhoff stress [44],

$$\hat{\mathbf{S}} = \begin{bmatrix} \hat{\mathbf{S}} & \hat{0} & \hat{0} \\ \hat{0} & \hat{\mathbf{S}} & \hat{0} \\ \hat{0} & \hat{0} & \hat{\mathbf{S}} \end{bmatrix}; \quad \hat{\mathbf{S}} = \begin{bmatrix} \mathbf{S}_{11} & \mathbf{S}_{12} & \mathbf{S}_{13} \\ \mathbf{S}_{12} & \mathbf{S}_{22} & \mathbf{S}_{23} \\ \mathbf{S}_{13} & \mathbf{S}_{23} & \mathbf{S}_{33} \end{bmatrix}; \quad \hat{0} = \begin{bmatrix} 0 & 0 & 0 \\ 0 & 0 & 0 \\ 0 & 0 & 0 \end{bmatrix}. \quad (\text{A.6})$$

Additionally, \mathbf{B}_L and \mathbf{B}_{NL} are defined as derivatives of the isoparametric shape functions with respect to the reference coordinates [44].

$$\mathbf{B}_L = \begin{bmatrix} \mathbf{F}_{11} \frac{\partial N_1}{\partial \mathbf{X}_1} & \mathbf{F}_{21} \frac{\partial N_1}{\partial \mathbf{X}_1} & \mathbf{F}_{31} \frac{\partial N_1}{\partial \mathbf{X}_1} & \mathbf{F}_{11} \frac{\partial N_2}{\partial \mathbf{X}_1} & \cdots & \mathbf{F}_{31} \frac{\partial N_n}{\partial \mathbf{X}_1} \\ \mathbf{F}_{12} \frac{\partial N_1}{\partial \mathbf{X}_2} & \mathbf{F}_{22} \frac{\partial N_1}{\partial \mathbf{X}_2} & \mathbf{F}_{32} \frac{\partial N_1}{\partial \mathbf{X}_2} & \mathbf{F}_{12} \frac{\partial N_2}{\partial \mathbf{X}_2} & \cdots & \mathbf{F}_{32} \frac{\partial N_n}{\partial \mathbf{X}_2} \\ \mathbf{F}_{13} \frac{\partial N_1}{\partial \mathbf{X}_3} & \mathbf{F}_{23} \frac{\partial N_1}{\partial \mathbf{X}_3} & \mathbf{F}_{33} \frac{\partial N_1}{\partial \mathbf{X}_3} & \mathbf{F}_{13} \frac{\partial N_2}{\partial \mathbf{X}_3} & \cdots & \mathbf{F}_{33} \frac{\partial N_n}{\partial \mathbf{X}_3} \\ \mathbf{F}_{11} \frac{\partial N_1}{\partial \mathbf{X}_2} + \mathbf{F}_{12} \frac{\partial N_1}{\partial \mathbf{X}_1} & \mathbf{F}_{21} \frac{\partial N_1}{\partial \mathbf{X}_2} + \mathbf{F}_{22} \frac{\partial N_1}{\partial \mathbf{X}_1} & \mathbf{F}_{31} \frac{\partial N_1}{\partial \mathbf{X}_2} + \mathbf{F}_{32} \frac{\partial N_1}{\partial \mathbf{X}_1} & \mathbf{F}_{11} \frac{\partial N_2}{\partial \mathbf{X}_2} + \mathbf{F}_{12} \frac{\partial N_2}{\partial \mathbf{X}_1} & \cdots & \mathbf{F}_{31} \frac{\partial N_n}{\partial \mathbf{X}_2} + \mathbf{F}_{32} \frac{\partial N_n}{\partial \mathbf{X}_1} \\ \mathbf{F}_{12} \frac{\partial N_1}{\partial \mathbf{X}_3} + \mathbf{F}_{13} \frac{\partial N_1}{\partial \mathbf{X}_1} & \mathbf{F}_{22} \frac{\partial N_1}{\partial \mathbf{X}_3} + \mathbf{F}_{23} \frac{\partial N_1}{\partial \mathbf{X}_2} & \mathbf{F}_{32} \frac{\partial N_1}{\partial \mathbf{X}_3} + \mathbf{F}_{33} \frac{\partial N_1}{\partial \mathbf{X}_2} & \mathbf{F}_{12} \frac{\partial N_2}{\partial \mathbf{X}_3} + \mathbf{F}_{13} \frac{\partial N_2}{\partial \mathbf{X}_2} & \cdots & \mathbf{F}_{32} \frac{\partial N_n}{\partial \mathbf{X}_3} + \mathbf{F}_{33} \frac{\partial N_n}{\partial \mathbf{X}_2} \\ \mathbf{F}_{11} \frac{\partial N_1}{\partial \mathbf{X}_3} + \mathbf{F}_{13} \frac{\partial N_1}{\partial \mathbf{X}_1} & \mathbf{F}_{21} \frac{\partial N_1}{\partial \mathbf{X}_3} + \mathbf{F}_{23} \frac{\partial N_1}{\partial \mathbf{X}_1} & \mathbf{F}_{31} \frac{\partial N_1}{\partial \mathbf{X}_3} + \mathbf{F}_{33} \frac{\partial N_1}{\partial \mathbf{X}_1} & \mathbf{F}_{11} \frac{\partial N_2}{\partial \mathbf{X}_3} + \mathbf{F}_{13} \frac{\partial N_2}{\partial \mathbf{X}_1} & \cdots & \mathbf{F}_{31} \frac{\partial N_n}{\partial \mathbf{X}_3} + \mathbf{F}_{33} \frac{\partial N_n}{\partial \mathbf{X}_1} \end{bmatrix} \quad (A.7)$$

$$\mathbf{B}_{NL} = \begin{bmatrix} \mathbf{B}_{NL} & \mathbf{0} & \mathbf{0} \\ \mathbf{0} & \mathbf{B}_{NL} & \mathbf{0} \\ \mathbf{0} & \mathbf{0} & \mathbf{B}_{NL} \end{bmatrix}; \quad \tilde{\mathbf{B}}_{NL} = \begin{bmatrix} \frac{\partial N_1}{\partial \mathbf{X}_1} & 0 & 0 & \frac{\partial N_2}{\partial \mathbf{X}_1} & \cdots & \frac{\partial N_n}{\partial \mathbf{X}_1} \\ \frac{\partial N_1}{\partial \mathbf{X}_2} & 0 & 0 & \frac{\partial N_2}{\partial \mathbf{X}_2} & \cdots & \frac{\partial N_n}{\partial \mathbf{X}_2} \\ \frac{\partial N_1}{\partial \mathbf{X}_3} & 0 & 0 & \frac{\partial N_2}{\partial \mathbf{X}_3} & \cdots & \frac{\partial N_n}{\partial \mathbf{X}_3} \end{bmatrix}; \quad \mathbf{0} = \begin{bmatrix} 0 \\ 0 \\ 0 \end{bmatrix}. \quad (A.8)$$

A.2. Updated lagrangian formulation

Similar to the total lagrangian formulation, the linearized updated lagrangian weak form equation is presented as [45],

$$\int_v \delta \mathbf{e}[\delta \mathbf{u}] : \boldsymbol{\epsilon} : \mathbf{e}[\mathbf{u}] dv + \int_v \sigma : [(\nabla \mathbf{u})^T \nabla \delta \mathbf{u}] dv = \int_{\partial v} \mathbf{t} \cdot \delta \mathbf{u} da + \int_v \mathbf{b} \cdot \delta \mathbf{u} dv \quad (A.9)$$

where all the components are associated with the current configuration. The final matrix form reads [44],

$$\begin{aligned} (\mathbf{K}_L + \mathbf{K}_{NL}) \mathbf{u} &= \mathbf{R} - \mathbf{R}_i, \\ \mathbf{K}_L &= \int_v \mathbf{B}_L^T \bar{\mathbf{c}} B_L dv, \\ \mathbf{K}_{NL} &= \int_v \mathbf{B}_{NL}^T \hat{\sigma} \mathbf{B}_{NL} dv, \\ \mathbf{R} &= \int_{\partial v} \mathbf{t} \cdot \delta \mathbf{u} da + \int_v \mathbf{b} \cdot \delta \mathbf{u} dv, \\ \mathbf{R}_i &= \int_v \mathbf{B}_L \hat{\sigma} dv, \end{aligned} \quad (A.10)$$

where the 6×6 elastic matrix $\bar{\mathbf{c}}$ is obtained from the minor and the major symmetry of the fourth order elastic tensor $\boldsymbol{\epsilon}$. Furthermore, $\hat{\sigma}$ is a 9×9 matrix achieved from the symmetric Cauchy stress as follows [44],

$$\hat{\sigma} = \begin{bmatrix} \hat{\sigma} & \hat{0} & \hat{0} \\ \hat{0} & \hat{\sigma} & \hat{0} \\ \hat{0} & \hat{0} & \hat{\sigma} \end{bmatrix}; \quad \hat{\sigma} = \begin{bmatrix} \sigma_{11} & \sigma_{12} & \sigma_{13} \\ \sigma_{12} & \sigma_{22} & \sigma_{23} \\ \sigma_{13} & \sigma_{23} & \sigma_{33} \end{bmatrix}; \quad \hat{0} = \begin{bmatrix} 0 & 0 & 0 \\ 0 & 0 & 0 \\ 0 & 0 & 0 \end{bmatrix}. \quad (A.11)$$

According to the current configuration, derivatives of the isoparametric shape function \mathbf{B}_L and \mathbf{B}_{NL} are defined as [44],

$$\mathbf{B}_L = \begin{bmatrix} \frac{\partial N_1}{\partial \mathbf{x}_1} & 0 & 0 & \frac{\partial N_2}{\partial \mathbf{x}_1} & \cdots & 0 \\ 0 & \frac{\partial N_1}{\partial \mathbf{x}_2} & 0 & 0 & \cdots & 0 \\ 0 & 0 & \frac{\partial N_1}{\partial \mathbf{x}_3} & 0 & \cdots & \frac{\partial N_n}{\partial \mathbf{x}_3} \\ \frac{\partial N_1}{\partial \mathbf{x}_2} & \frac{\partial N_1}{\partial \mathbf{x}_1} & 0 & \frac{\partial N_2}{\partial \mathbf{x}_2} & \cdots & 0 \\ 0 & \frac{\partial N_1}{\partial \mathbf{x}_3} & \frac{\partial N_1}{\partial \mathbf{x}_2} & 0 & \cdots & \frac{\partial N_n}{\partial \mathbf{x}_2} \\ \frac{\partial N_1}{\partial \mathbf{x}_3} & 0 & \frac{\partial N_1}{\partial \mathbf{x}_1} & \frac{\partial N_2}{\partial \mathbf{x}_3} & \cdots & \frac{\partial N_n}{\partial \mathbf{x}_1} \end{bmatrix} \quad (\text{A.12})$$

$$\mathbf{B}_{NL} = \begin{bmatrix} \tilde{\mathbf{B}}_{NL} & \tilde{0} & \tilde{0} \\ \tilde{0} & \tilde{\mathbf{B}}_{NL} & \tilde{0} \\ \tilde{0} & \tilde{0} & \tilde{\mathbf{B}}_{NL} \end{bmatrix}; \quad \mathbf{B}_{NL} = \begin{bmatrix} \frac{\partial N_1}{\partial \mathbf{x}_1} & 0 & 0 & \frac{\partial N_2}{\partial \mathbf{x}_1} & \cdots & \frac{\partial N_n}{\partial \mathbf{x}_1} \\ \frac{\partial N_1}{\partial \mathbf{x}_2} & 0 & 0 & \frac{\partial N_2}{\partial \mathbf{x}_2} & \cdots & \frac{\partial N_n}{\partial \mathbf{x}_2} \\ \frac{\partial N_1}{\partial \mathbf{x}_3} & 0 & 0 & \frac{\partial N_2}{\partial \mathbf{x}_3} & \cdots & \frac{\partial N_n}{\partial \mathbf{x}_3} \end{bmatrix}; \quad \tilde{0} = \begin{bmatrix} 0 \\ 0 \\ 0 \end{bmatrix}. \quad (\text{A.13})$$

Appendix B. Second Piola–Kirchhoff stress and elasticity tensor

In this section, the focus is set on calculating derivatives of Eq. (30) which are exploited directly in the stiffness matrix. Based on Eq. (24), the second Piola–Kirchhoff stress in material description reads as,

$$\begin{aligned} \mathbf{S} = & K I_3^{-1} \ln(J) I_{3,\mathbf{E}} + (1 - D_m) \left\{ c_1 \tilde{I}_{1,\mathbf{E}} + c_2 \tilde{I}_{2,\mathbf{E}} \right\} \\ & + (1 - D_{f_i}) c_3 \left(\tilde{I}_{f_i,\mathbf{E}} - I_{0_i} \right) \left\{ \exp \left[c_4 \left(\kappa_i \tilde{I}_1 + [1 - 3\kappa_i] \tilde{I}_{f_i} - I_{0_i} \right) \right] \right\} \\ & \times \left(\kappa_i \tilde{I}_{1,\mathbf{E}} + [1 - 3\kappa_i] \tilde{I}_{f_i,\mathbf{E}} \right) \quad i = 1, 2. \end{aligned} \quad (\text{B.1})$$

The deviatoric part of the invariants and their derivatives are presented as [62]

$$\tilde{I}_1 = I_3^{-1/3} I_1, \quad \tilde{I}_2 = I_3^{-2/3} I_2, \quad \tilde{I}_{f_1} = \tilde{I}_4 = I_3^{-1/3} I_4, \quad \tilde{I}_{f_2} = \tilde{I}_6 = I_3^{-1/3} I_6 \quad (\text{B.2})$$

$$\tilde{I}_{1,\mathbf{E}} = I_3^{-1/3} I_{1,\mathbf{E}} - \frac{1}{3} I_1 I_3^{-4/3} I_{3,\mathbf{E}} \quad (\text{B.3a})$$

$$\tilde{I}_{2,\mathbf{E}} = I_3^{-2/3} I_{2,\mathbf{E}} - \frac{2}{3} I_2 I_3^{-5/3} I_{3,\mathbf{E}} \quad (\text{B.3b})$$

$$\tilde{I}_{4,\mathbf{E}} = I_3^{-1/3} I_{4,\mathbf{E}} - \frac{1}{3} I_4 I_3^{-4/3} I_{3,\mathbf{E}} \quad (\text{B.3c})$$

$$\tilde{I}_{6,\mathbf{E}} = I_3^{-1/3} I_{6,\mathbf{E}} - \frac{1}{3} I_6 I_3^{-4/3} I_{3,\mathbf{E}} \quad (\text{B.3d})$$

where

$$I_{1,\mathbf{E}} = 2\mathbf{1} = 2 \begin{bmatrix} 1 & 0 & 0 \\ 0 & 1 & 0 \\ 0 & 0 & 1 \end{bmatrix} \quad (\text{B.4a})$$

$$I_{2,\mathbf{E}} = 2\{I_1\mathbf{1} - \mathbf{C}\} = 2 \begin{bmatrix} \mathbf{C}_{22} + \mathbf{C}_{33} & -\mathbf{C}_{12} & -\mathbf{C}_{13} \\ -\mathbf{C}_{12} & \mathbf{C}_{33} + \mathbf{C}_{11} & -\mathbf{C}_{23} \\ -\mathbf{C}_{13} & -\mathbf{C}_{23} & \mathbf{C}_{11} + \mathbf{C}_{22} \end{bmatrix} \quad (\text{B.4b})$$

$$I_{3,\mathbf{E}} = 2I_3\mathbf{C}^{-1} \quad (\text{B.4c})$$

$$I_{4,\mathbf{E}} = 2\mathbf{M} \quad (\text{B.4d})$$

$$I_{6,\mathbf{E}} = 2\mathbf{N}. \quad (\text{B.4e})$$

The corresponding elasticity tensor based on Eq. (26) is presented in the material description as,

$$\begin{aligned} \mathcal{C} = & K \left\{ I_3^{-2} (1/2 - \ln J) I_{3,\mathbf{E}} \otimes I_{3,\mathbf{E}} + I_3^{-1} \ln(J) I_{3,\mathbf{EE}} \right\} + (1 - D_m) \left\{ c_1 \tilde{I}_{1,\mathbf{EE}} + c_2 \tilde{I}_{2,\mathbf{EE}} \right\} \\ & + c_3 (1 - D_{f_i}) \exp \left[c_4 \left(\kappa_i \tilde{I}_1 + [1 - 3\kappa_i] \tilde{I}_{f_i} - I_{0_i} \right) \right] \left\{ \kappa_i \tilde{I}_{f_i,\mathbf{E}} \otimes \tilde{I}_{1,\mathbf{E}} + [1 - 3\kappa_i] \tilde{I}_{f_i,\mathbf{E}} \otimes \tilde{I}_{f_i,\mathbf{E}} \right. \\ & \left. + c_4 (\tilde{I}_{f_i,\mathbf{E}} - I_{0_i}) \left[\kappa_i^2 \tilde{I}_{1,\mathbf{E}} \otimes \tilde{I}_{1,\mathbf{E}} + \kappa_i [1 - 3\kappa_i] [\tilde{I}_{1,\mathbf{E}} \otimes \tilde{I}_{f_i,\mathbf{E}} + \tilde{I}_{f_i,\mathbf{E}} \otimes \tilde{I}_{1,\mathbf{E}}] \right. \right. \\ & \left. \left. + [1 - 3\kappa_i]^2 \tilde{I}_{f_i,\mathbf{E}} \otimes \tilde{I}_{f_i,\mathbf{E}} \right] + (\tilde{I}_{f_i,\mathbf{E}} - I_{0_i}) \left[\kappa_i \tilde{I}_{1,\mathbf{EE}} + [1 - 3\kappa_i] \tilde{I}_{f_i,\mathbf{EE}} \right] \right\} \quad i = 1, 2 \end{aligned} \quad (\text{B.5})$$

where

$$\tilde{I}_{1,\mathbf{EE}} = -2/3I_3^{-1/2} \left(\tilde{I}_{1,\mathbf{E}} \otimes \tilde{I}_{3,\mathbf{E}} + \tilde{I}_{3,\mathbf{E}} \otimes \tilde{I}_{1,\mathbf{E}} \right) + I_1 I_3^{-4/3} \left\{ 8/9 \tilde{I}_{3,\mathbf{E}} \otimes \tilde{I}_{3,\mathbf{E}} - 1/3 I_{3,\mathbf{EE}} \right\} \quad (\text{B.6a})$$

$$\begin{aligned} \tilde{I}_{2,\mathbf{EE}} = & 4/3I_3^{-1/2} \left(\tilde{I}_{2,\mathbf{E}} \otimes \tilde{I}_{3,\mathbf{E}} + \tilde{I}_{3,\mathbf{E}} \otimes \tilde{I}_{2,\mathbf{E}} \right) + 8/9I_2 I_3^{-5/3} \left(\tilde{I}_{3,\mathbf{E}} \otimes \tilde{I}_{3,\mathbf{E}} \right) + I_3^{-2/3} I_{2,\mathbf{EE}} \\ & - 2/3I_2 I_3^{-5/3} I_{3,\mathbf{EE}} \end{aligned} \quad (\text{B.6b})$$

$$\tilde{I}_{3,\mathbf{EE}} = -I_3^{-1/2} \left\{ \tilde{I}_{3,\mathbf{E}} \otimes \tilde{I}_{3,\mathbf{E}} - 1/2 I_{3,\mathbf{EE}} \right\} \quad (\text{B.6c})$$

$$\tilde{I}_{4,\mathbf{EE}} = -2/3I_3^{-1/2} \left(\tilde{I}_{4,\mathbf{E}} \otimes \tilde{I}_{3,\mathbf{E}} + \tilde{I}_{3,\mathbf{E}} \otimes \tilde{I}_{4,\mathbf{E}} \right) + I_4 I_3^{-4/3} \left\{ 8/9 \tilde{I}_{3,\mathbf{E}} \otimes \tilde{I}_{3,\mathbf{E}} - 1/3 I_{3,\mathbf{EE}} \right\} \quad (\text{B.6d})$$

$$\tilde{I}_{6,\mathbf{EE}} = -2/3I_3^{-1/2} \left(\tilde{I}_{6,\mathbf{E}} \otimes \tilde{I}_{3,\mathbf{E}} + \tilde{I}_{3,\mathbf{E}} \otimes \tilde{I}_{6,\mathbf{E}} \right) + I_6 I_3^{-4/3} \left\{ 8/9 \tilde{I}_{3,\mathbf{E}} \otimes \tilde{I}_{3,\mathbf{E}} - 1/3 I_{3,\mathbf{EE}} \right\} \quad (\text{B.6e})$$

$$I_{2,\mathbf{EE}} = 4 \{ \mathbf{1} \otimes \mathbf{1} - \widehat{\mathbf{I}} \}, \quad \widehat{\mathbf{I}}_{ijkl} = 1/2 \{ \delta_{ik} \delta_{jl} + \delta_{il} \delta_{jk} \}, \quad \delta_{ij} = \begin{cases} 1 & i = j \\ 0 & i \neq j \end{cases} \quad (\text{B.6f})$$

$$I_{3,\mathbf{EE}} = 4I_3 \left\{ \mathbf{C}^{-1} \otimes \mathbf{C}^{-1} - \widehat{\mathbf{I}} \right\}, \quad \widehat{\mathbf{I}}_{ijkl} = 1/2 \left\{ \mathbf{C}_{ik}^{-1} \mathbf{C}_{jl}^{-1} + \mathbf{C}_{il}^{-1} \mathbf{C}_{jk}^{-1} \right\}. \quad (\text{B.6g})$$

References

- [1] T.C. Gasser, R.W. Ogden, G.A. Holzapfel, Hyperelastic modelling of arterial layers with distributed collagen fibre orientations, *J. R. Soc. Interface* 3 (2006) 15–35.
- [2] A.N. Annaidh, K. Bruyere, M. Destrade, M.D. Gilchrist, C. Maurini, M. Otténo, G. Saccomandi, Automated estimation of collagen fibre dispersion in the dermis and its contribution to the anisotropic behaviour of skin, *Ann. Biomed. Eng.* 40 (2012) 1666–1678.
- [3] V. Alastrué, J. Rodríguez, B. Calvo, M. Doblaré, Structural damage models for fibrous biological soft tissues, *Int. J. Solids Struct.* 44 (2007) 5894–5911.
- [4] H. Demiray, A note on the elasticity of soft biological tissues, *J. Biomech.* 5 (1972) 309–311.
- [5] M. Mooney, A theory of large elastic deformation, *J. Appl. Phys.* 11 (1940) 582–592.
- [6] R. Katzengold, M. Topaz, A. Gefen, Tissue loads applied by a novel medical device for closing large wounds, *J. Tissue Viability* 25 (2016) 32–40.
- [7] D. Balzani, P. Neff, J. Schröder, G.A. Holzapfel, A polyconvex framework for soft biological tissues. Adjustment to experimental data, *Internat. J. Solids Structures* 43 (2006) 6052–6070.

- [8] P. Fratzl, R. Weinkamer, Nature's hierarchical materials, *Prog. Mater. Sci.* 52 (2007) 1263–1334.
- [9] M. Itskov, A. Ehret, D. Mavrilas, A polyconvex anisotropic strain-energy function for soft collagenous tissues, *Biomech. Model. Mechanobiol.* 5 (2006) 17–26.
- [10] Y.-c. Fung, Mechanical properties and active remodeling of blood vessels, in: *Biomechanics*, Springer, 1993, pp. 321–391.
- [11] E. Peña, Prediction of the softening and damage effects with permanent set in fibrous biological materials, *J. Mech. Phys. Solids* 59 (2011) 1808–1822.
- [12] G.A. Holzapfel, M. Stadler, T.C. Gasser, Changes in the mechanical environment of stenotic arteries during interaction with stents: computational assessment of parametric stent designs, *J. Biomech. Eng.* 127 (2005) 166–180.
- [13] I. Pericevic, C. Lally, D. Toner, D.J. Kelly, The influence of plaque composition on underlying arterial wall stress during stent expansion: the case for lesion-specific stents, *Med. Eng. Phys.* 31 (2009) 428–433.
- [14] G.A. Holzapfel, M. Stadler, C.A. Schulze-Bauer, A layer-specific three-dimensional model for the simulation of balloon angioplasty using magnetic resonance imaging and mechanical testing, *Ann. Biomed. Eng.* 30 (2002) 753–767.
- [15] J. Ju, On energy-based coupled elastoplastic damage theories: constitutive modeling and computational aspects, *Int. J. Solids Struct.* 25 (1989) 803–833.
- [16] M. Jirásek, Non-local damage mechanics with application to concrete, *Rev. Fr. Génie Civ.* 8 (2004) 683–707.
- [17] C. Comi, S. Mariani, U. Perego, An extended FE strategy for transition from continuum damage to mode I cohesive crack propagation, *Int. J. Numer. Anal. Methods Geomech.* 31 (2007) 213–238.
- [18] D. Edelen, A. Green, N. Laws, Nonlocal continuum mechanics, *Arch. Ration. Mech. Anal.* 43 (1971) 36–44.
- [19] A.C. Eringen, Linear theory of nonlocal elasticity and dispersion of plane waves, *Internat. J. Engrg. Sci.* 10 (1972) 425–435.
- [20] A.C. Eringen, *Nonlocal Continuum Field Theories*, Springer Science & Business Media, 2002.
- [21] A.C. Eringen, D. Edelen, On nonlocal elasticity, *Internat. J. Engrg. Sci.* 10 (1972) 233–248.
- [22] Z.P. Bazant, F.-B. Lin, Nonlocal smeared cracking model for concrete fracture, *J. Struct. Eng.* 114 (1988) 2493–2510.
- [23] M. Jirásek, T. Zimmermann, Rotating crack model with transition to scalar damage: I. Local formulation, II. Nonlocal formulation and adaptivity, in: *LSC Internal Report 97 = 01*, Swiss Federal Institute of Technology at Lausanne, Switzerland, 1997.
- [24] Z. Bažant, F.B. Lin, Non-local yield limit degradation, *Internat. J. Numer. Methods Engrg.* 26 (1988) 1805–1823.
- [25] R. Peerlings, R. De Borst, W. Brekelmans, M. Geers, Gradient-enhanced damage modelling of concrete fracture, *Mech. Cohes.-Frict. Mater.* 3 (1998) 323–342.
- [26] E. Kuhl, E. Ramm, Simulation of strain localization with gradient enhanced damage models, *Comput. Mater. Sci.* 16 (1999) 176–185.
- [27] E. Kuhl, E. Ramm, R. de Borst, An anisotropic gradient damage model for quasi-brittle materials, *Comput. Methods Appl. Mech. Engrg.* 183 (2000) 87–103.
- [28] D. Lasry, T. Belytschko, Localization limiters in transient problems, *Internat. J. Solids Structures* 24 (1988) 581–597.
- [29] T. Waffenschmidt, C. Polindara, A. Menzel, S. Blanco, A gradient-enhanced large-deformation continuum damage model for fibre-reinforced materials, *Comput. Methods Appl. Mech. Engrg.* 268 (2014) 801–842.
- [30] C. Miehe, F. Welschinger, M. Hofacker, Thermodynamically consistent phase-field models of fracture: Variational principles and multi-field FE implementations, *Internat. J. Numer. Methods Engrg.* 83 (2010) 1273–1311.
- [31] V. Hakim, A. Karma, Laws of crack motion and phase-field models of fracture, *J. Mech. Phys. Solids* 57 (2009) 342–368.
- [32] O. Gültkin, H. Dal, G.A. Holzapfel, A phase-field approach to model fracture of arterial walls: theory and finite element analysis, *Comput. Methods Appl. Mech. Engrg.* 312 (2016) 542–566.
- [33] J. Simo, On a fully three-dimensional finite-strain viscoelastic damage model: formulation and computational aspects, *Comput. Methods Appl. Mech. Engrg.* 60 (1987) 153–173.
- [34] D. Balzani, J. Schröder, D. Gross, Simulation of discontinuous damage incorporating residual stresses in circumferentially overstretched atherosclerotic arteries, *Acta Biomater.* 2 (2006) 609–618.
- [35] B. Calvo, E. Pena, M. Martinez, M. Doblaré, An uncoupled directional damage model for fibred biological soft tissues. Formulation and computational aspects, *Internat. J. Numer. Methods Engrg.* 69 (2007) 2036–2057.
- [36] E. Peña, A rate dependent directional damage model for fibred materials: application to soft biological tissues, *Comput. Mech.* 48 (2011) 407–420.
- [37] J. Simo, J. Ju, Strain-and stress-based continuum damage models—I. Formulation, *Internat. J. Solids Structures* 23 (1987) 821–840.
- [38] E.M. Arruda, M.C. Boyce, A three-dimensional constitutive model for the large stretch behavior of rubber elastic materials, *J. Mech. Phys. Solids* 41 (1993) 389–412.
- [39] E. Peña, J.A. Peña, M. Doblaré, On the Mullins effect and hysteresis of fibered biological materials: A comparison between continuous and discontinuous damage models, *Internat. J. Solids Structures* 46 (2009) 1727–1735.
- [40] A.E. Ehret, M. Itskov, Modeling of anisotropic softening phenomena: application to soft biological tissues, *Int. J. Plast.* 25 (2009) 901–919.
- [41] D. Balzani, S. Brinkhues, G.A. Holzapfel, Constitutive framework for the modeling of damage in collagenous soft tissues with application to arterial walls, *Comput. Methods Appl. Mech. Engrg.* 213 (2012) 139–151.
- [42] L.J. Sluys, *Wave Propagation, Localisation and Dispersion in Softening Solids*, TU Delft, Delft University of Technology, 1992.
- [43] D. Balzani, M. Ortiz, Relaxed incremental variational formulation for damage at large strains with application to fiber-reinforced materials and materials with truss-like microstructures, *Internat. J. Numer. Methods Engrg.* 92 (2012) 551–570.
- [44] K.-J. Bathe, *Finite element procedures*, Klaus-Jürgen Bathe, 2006.
- [45] J. Bonet, R.D. Wood, *Nonlinear Continuum Mechanics for Finite Element Analysis*, Cambridge University Press, 1997.
- [46] M.S. Sacks, D.C. Goeckner, Quantification of the fiber architecture and biaxial mechanical behavior of porcine intestinal submucosa, *J. Biomed. Mater. Res.* 46 (1999) 1–10.
- [47] G.A. Holzapfel, *Nonlinear Solid Mechanics*, Wiley, Chichester, 2000.
- [48] E. Peña, Damage functions of the internal variables for soft biological fibred tissues, *Mech. Res. Comm.* 38 (2011) 610–615.
- [49] K. Volokh, Prediction of arterial failure based on a microstructural bi-layer fiber–matrix model with softening, *J. Biomech.* 41 (2008) 447–453.

- [50] M. Jirásek, Nonlocal damage mechanics, *Rev. Eur. Génie Civ.* 11 (2007) 993–1021.
- [51] Z.P. Bazant, M. Jirásek, Nonlocal integral formulations of plasticity and damage: survey of progress, *J. Eng. Mech.* 128 (2002) 1119–1149.
- [52] R.A. Engelen, M.G. Geers, F.P. Baaijens, Nonlocal implicit gradient-enhanced elasto-plasticity for the modelling of softening behaviour, *Int. J. Plast.* 19 (2003) 403–433.
- [53] R. De Borst, J. Pamin, R. Peerlings, L. Sluys, On gradient-enhanced damage and plasticity models for failure in quasi-brittle and frictional materials, *Comput. Mech.* 17 (1995) 130–141.
- [54] R. Peerlings, M. Geers, R. De Borst, W. Brekelmans, A critical comparison of nonlocal and gradient-enhanced softening continua, *Int. J. Solids Struct.* 38 (2001) 7723–7746.
- [55] P. Martins, E. Pena, R.N. Jorge, A. Santos, L. Santos, T. Mascarenhas, B. Calvo, Mechanical characterization and constitutive modelling of the damage process in rectus sheath, *J. Mech. Behav. Biomed. Mater.* 8 (2012) 111–122.
- [56] J.A. Weiss, A constitutive model and finite element representation for transversely isotropic soft tissues, 1995.
- [57] A. Ferrara, A. Pandolfi, Numerical modelling of fracture in human arteries, *Comput. Methods Biomed. Eng.* 11 (2008) 553–567.
- [58] F.J. Criado, Aortic dissection: a 250-year perspective, *Tex. Heart Inst. J.* 38 (2011) 694.
- [59] T.C. Gasser, G.A. Holzapfel, Modeling the propagation of arterial dissection, *Eur. J. Mech.-A/Solids* 25 (2006) 617–633.
- [60] A. Ferrara, A. Pandolfi, A numerical study of arterial media dissection processes, *Int. J. Fract.* 166 (2010) 21–33.
- [61] G. Sommer, T.C. Gasser, P. Regitnig, M. Auer, G.A. Holzapfel, Dissection properties of the human aortic media: an experimental study, *J. Biomech. Eng.* 130 (2008) 021007.
- [62] N.-H. Kim, *Introduction to Nonlinear Finite Element Analysis*, Springer Science & Business Media, 2014.